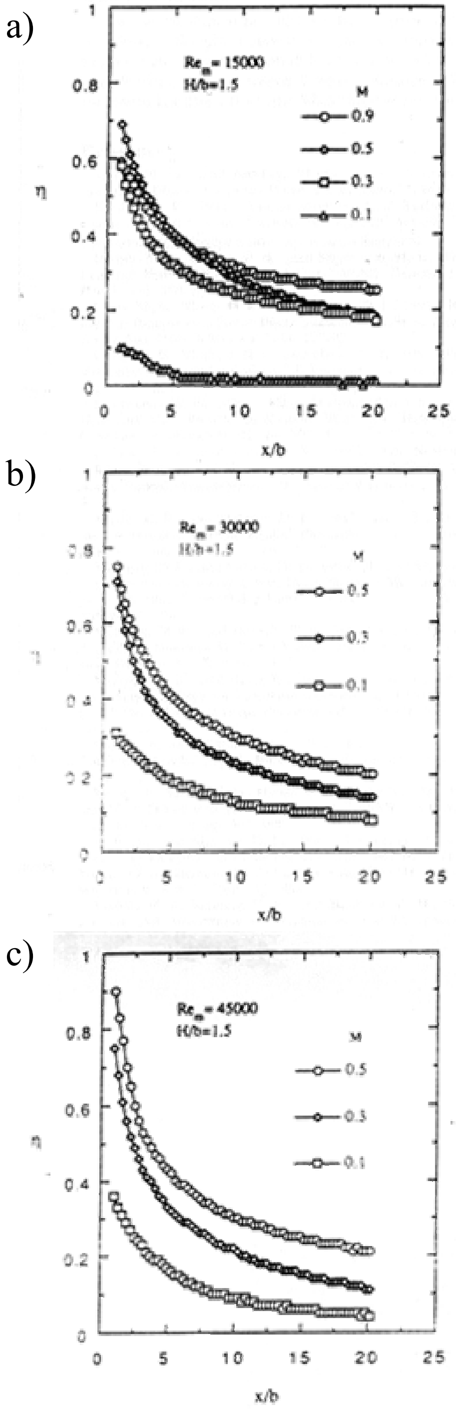

Figure 2-10 Spanwise averaged effectiveness for a) Re = 15,000 at four blowing ratios, b) Re = 30,000 at three blowing ratios, and c) Re = 45,000 at three blowing ratios (Kim and Metzger, 1995).

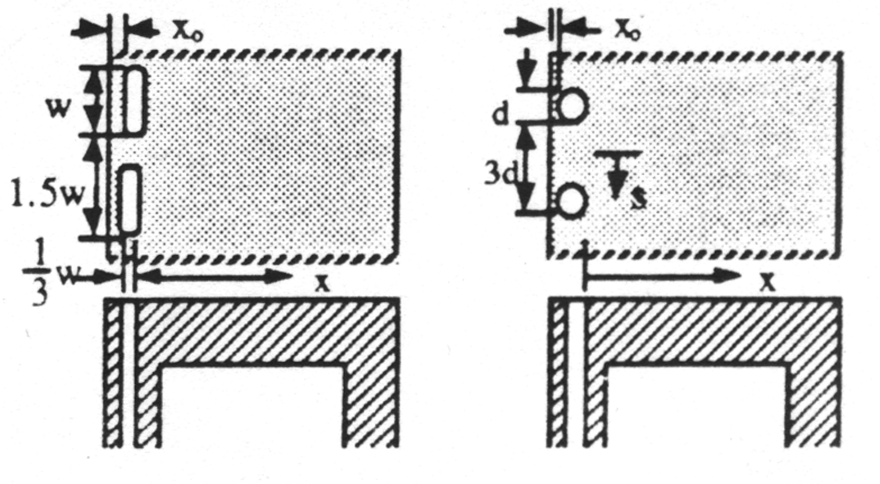

(a) Discrete Slot (b) Round Hole

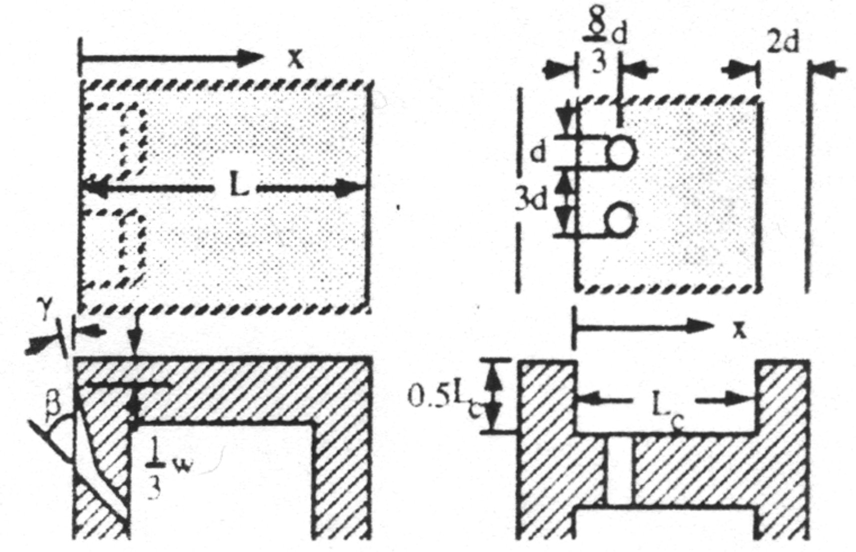

(c) Pressure Side (d) Grooved-Tip

Configuration	Dimensions (cm)
Discrete Slot	xo=0.25, w=0.95
Round Hole	xo=0.25, d=0.48
Pressure Side	w=0.95, γ=12°, β=45°
Grooved Tip	d=0.48, Lc=5.08

Figure 2-11 Heat transfer coefficients were examined for four different tip geometries including a) discrete slots, b) round holes, c) pressure side injection, and d) grooved tips (Kim et al., 1995).

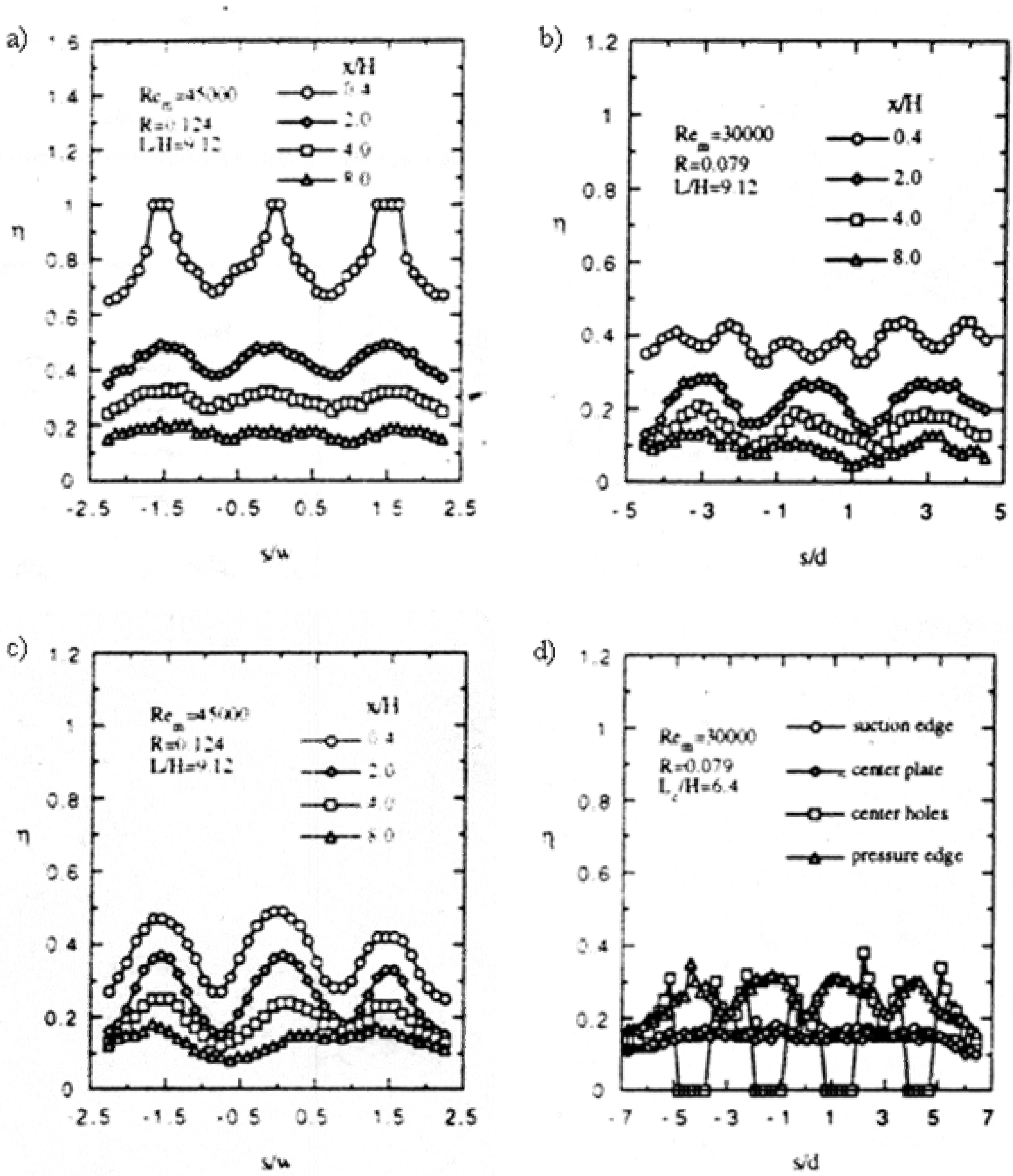

Figure 2-12 Typical spanwise film cooling effectiveness results at various locations downstream of the cooling ducts for a) discrete slots, b) round holes, c) pressure side injection, and d) grooved tips (Kim et al., 1995).

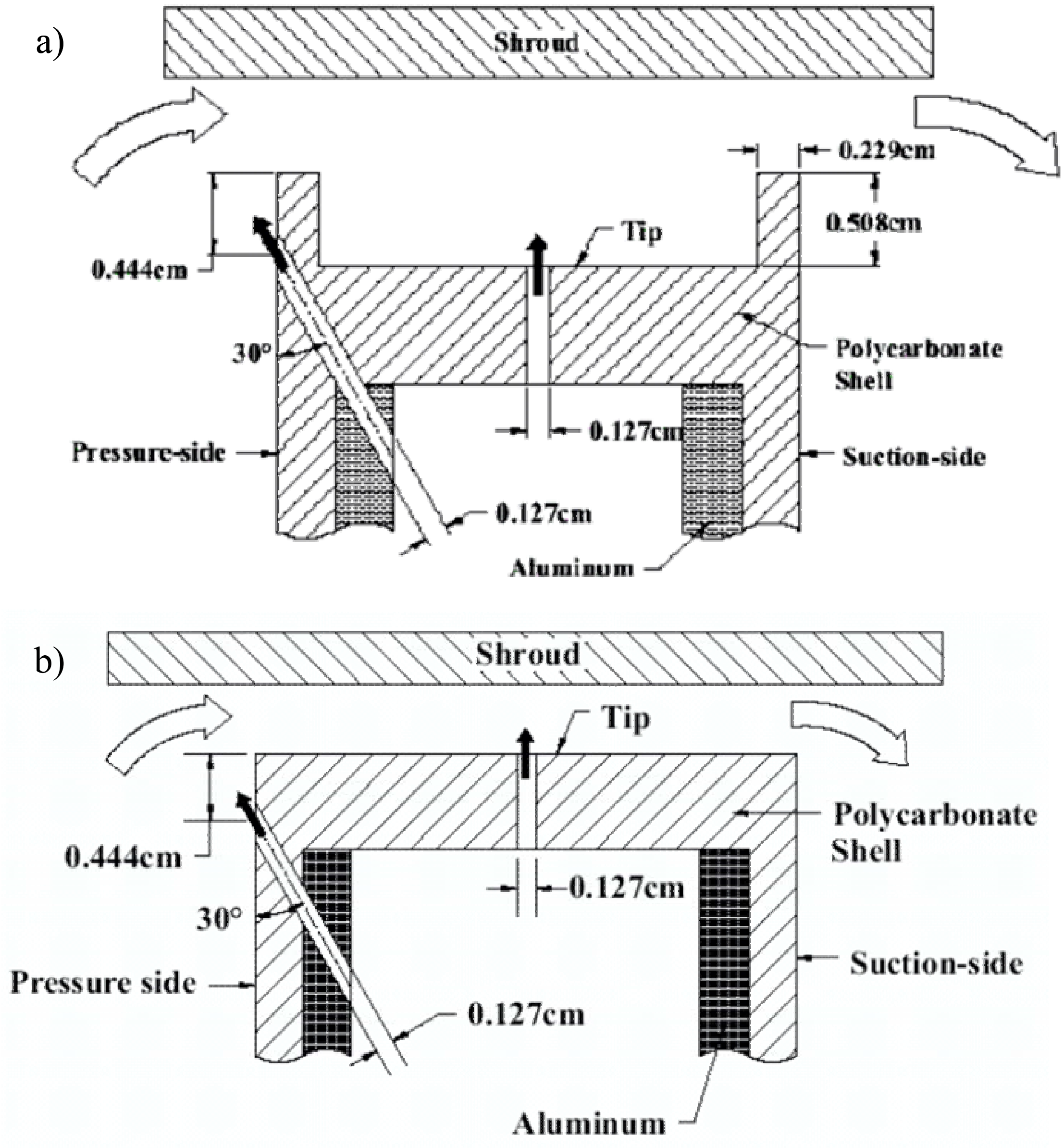

Figure 2-13 Film-cooling configurations shown a) with a squealer tip (Kwak and Han, 2002b) and b) flat tip (Kwak and Han, 2002a).

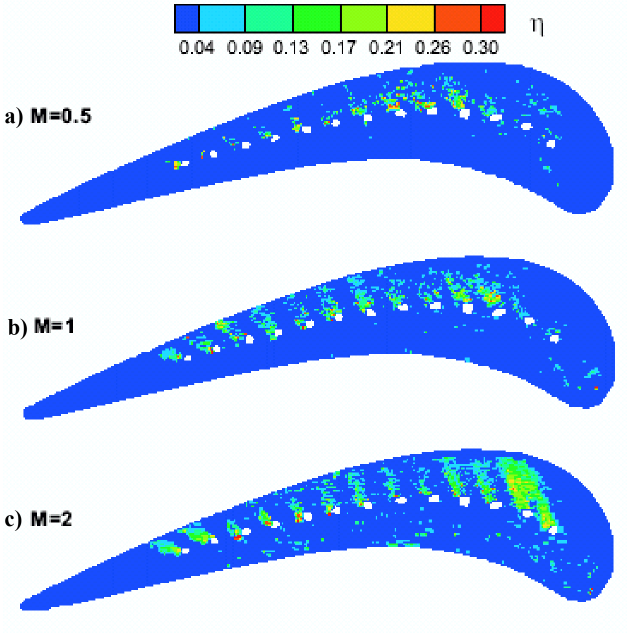

Figure 2-14 Film-cooling effectiveness contours for tip blowing over a flat tip with gap height at 1.5% of the total blade height and blowing ratios of a) M = 0.5, b) M = 1, and c) M = 2 (Kwak and Han, 2002a).

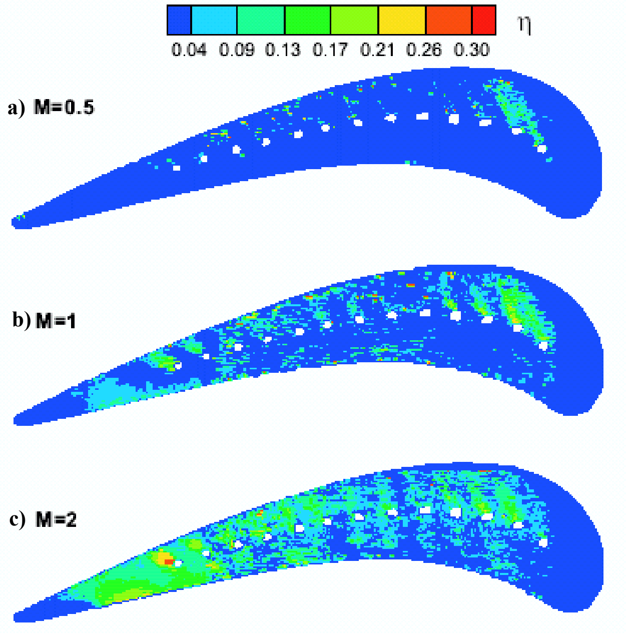

Figure 2-15 Film-cooling effectiveness contours for tip and pressure side blowing over a flat tip with gap height at 1.5% of the total blade height and blowing ratios of a) M = 0.5, b) M = 1, and c) M = 2 (Kwak and Han, 2002a).

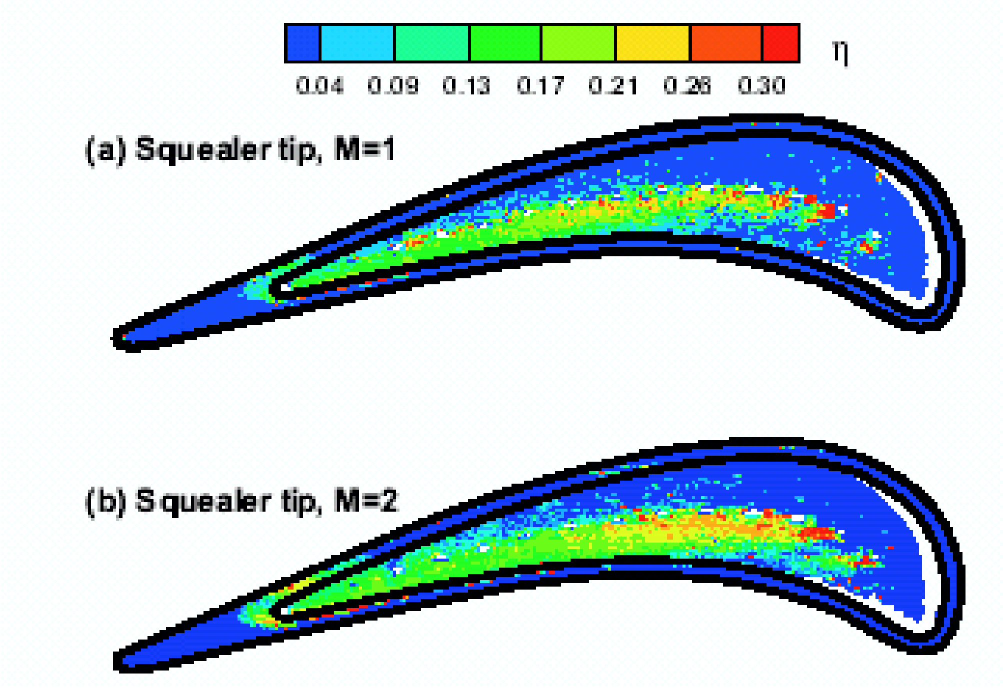

Figure 2-16 Film-cooling effectiveness contours for tip blowing over a squealer tip with blowing ratios of a) M = 1 and b) M = 2 (Kwak and Han, 2002b).

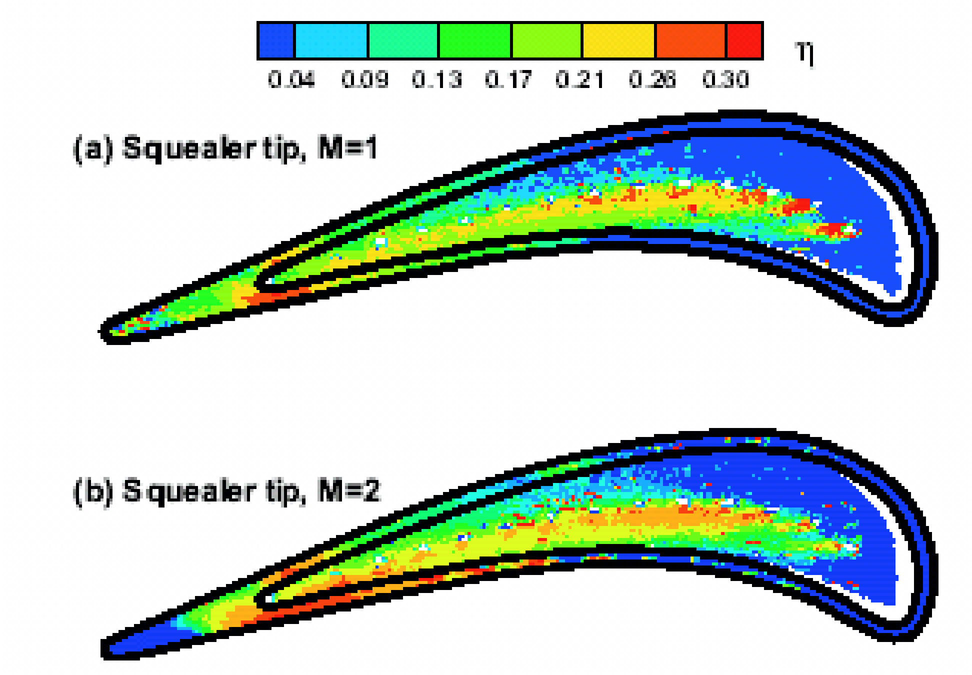

Figure 2-17 Film-cooling effectiveness contours for tip and pressure side blowing over a squealer tip with blowing ratios of a) M = 1 and b) M = 2 (Kwak and Han, 2002b).

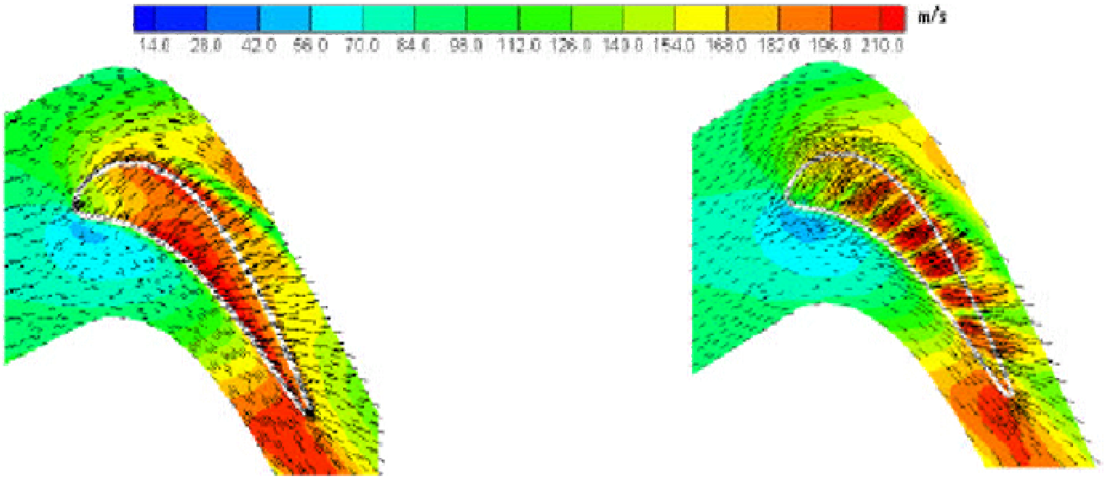

a) b)

Figure 2-18 Velocity vectors and magnitudes on the middle plane of tip gap with a gap clearance of 1.5% of the total blade height, turbulence levels of 6.1% for the cases a) without film-cooling and b) with film cooling (Acharya et al., 2002).

Chapter 3: Experimental Facilities and Instrumentation

The literature suggests that the tip region is one of complex three-dimensional flows that would be difficult to observe at true scale. Large scale testing can be an effective way of observing spatially-resolved details for the tip. The first section of this chapter describes the wind tunnel facility used in this study. It also discusses in detail the tip geometry to be tested and the wind tunnel section constructed to house this model. The next section discusses the measuring techniques used to acquire surface thermal data and static pressures on the shroud as well as the instrumentation involved. The third section outlines the tunnel flow settings used in this study and demonstrates repeatability in measurements. Finally, an analysis of uncertainty in the results is presented.

3.1 Wind Tunnel Facility

This section offers a description of the experimental facilities and models used in this study. Tests were conducted in the large scale, low speed wind tunnel depicted in Figure 3-1. The tunnel cycled air around a closed loop with a 50 hp, 0-60 Hz Joy Technologies axial fan. Air exiting the fan was cooled by a primary heat exchanger in which the operating fluid was water cooled by a 38 kW chiller. Using a refrigerant, this chiller circulated water from a reservoir that was maintained at a temperature specified by the user. The heat exchanger could also have used tap water, but the chiller was used so that the water temperature did not vary.

Following the primary heat exchanger, the flow split into three passages in the transition section. A perforated wooden plate, shown in Figure 3-1, was placed over the center passage providing the necessary pressure drop to distribute flow through all three passages. This plate had an open area of 0.269 m^2 or 24.6% of the main passage area. A 55 kW heater bank heated the center passage flow. The heater bank consisted of a top, middle, and bottom section, so that the power to each section could be independently adjusted through a digital control panel. During these experiments, the same power was allotted to each heater to provide an isothermal flowfield. The outer passages housed secondary heat exchangers, which could operate with chilled water or tap water to cool the air entering the combustor simulator. The exact settings for all of these thermal conditioning components are discussed in detail in Section 3.3.

Combustor Simulator. The combustor simulator is capable of modeling film cooling and injection cooling schemes by reintroducing the cooler flows from the outer passages to the hot flow in the center passage. Barringer et al. [2002] describe the design and benchmarking of the combustor simulator. We focused on the heat transfer at the blade tip, so the combustor simulator was not used for its intended purpose. The only feature used was a single row of dilution jets on the bottom of the simulator that provided a high turbulence inlet condition.

While the top passage was not used in these experiments, air from the bottom passage was injected into the center passage through three 8.5 cm (3.35 in) diameter dilution holes. The holes were located 2.1 chords upstream of the combustor simulator exit. The center dilution hole was positioned in the center of the tunnel directly upstream of the stagnation location of the test blade. The other two dilution holes were spaced 1.1 pitches on either side of the center hole.

Just upstream of the blades, the combustor simulator height contracted at an angle of 15.4° from 98 cm (38.6 in) to 55 cm (21.8 in) while the width remained 112 cm (44 in). Though the dilution flow provided turbulence upstream of the blade, there was concern that the transition from the combustor simulator to the test section inlet would cause a small laminar boundary layer at the tip gap. A 1.6 mm (0.063 in) diameter brass tube was made to run along the floor upstream of the blades to trip this laminar flow and ensure a turbulent boundary layer at the tip gap. Figure 3-2 shows pressure distributions on the shroud indicating that this trip wire had no noticeable effect on the flow field through the tip gap.

The combustor simulator exit was a 112 cm x 55 cm (44.1 in x 21.8 in) opening, and a tunnel section housing the test blades was built to meet up to this opening. The tip gap to be studied was located near the floor of the tunnel, so a smooth transition from the combustor exit to the test section inlet was achieved with a sheet of 1.6 mm (0.063 in) thick Formica. The Formica sheet extended 45.0 cm (17.72 in) into the contraction of the combustor simulator and 11.5 cm (4.53 in) into the level floor of the test section.

Coolant Supply. The tip geometries that were tested required a coolant air supply at temperatures below that of the air exiting the combustor simulator. This air was supplied by two external tanks, which were pressurized by compressors. The first tank was located at the Virginia Tech Power Plant (Long, 2002) and was used to provide compressed air to lines throughout the Virginia Tech campus. This tank was automatically recharged at the power plant to maintain a supply pressure of 551.6 kPa (80 psi). The second tank, located in the Aerospace Department of Randolph Hall (Edwards, 2002), was used as a supplementary air supply for cases that required more flow than the first tank alone could provide. This tank was typically pressurized to 14.4 kPa (300 psi). For the highest flow cases, the pressure in the second tank would drop about 50 psi over an hour, and we would activate the compressor to recharge the tank as needed. As a safety precaution, the line from this tank had a regulator at the wind tunnel location that could reduce the supply pressure to as little as 68.9 kPa (10 psi). Dryers removed moisture from both tanks, which supplied air at ambient temperatures. The tanks delivered coolant to the blade tip through the piping circuit illustrated in Figure 3-3. The pipe connectors used were all standard polyvinyl chloride (PVC) pipe components with a 7.6 cm (3.0 in) internal diameter (ID).

To measure the coolant flowrate, a 0-2491 Pa (0-10 inH$_2$O) transducer displayed the pressure drop across a venturi tube in the PVC pipe circuit. The model CV-150 venturi tube was manufactured by Lambda Square, Incorporated. The pressure drop across the venturi tube was correlated to a flowrate using a formula provided by Lambda Square. The manufacturer recommended that a constant area flow be maintained at least five diameters upstream of the venturi tube. The tube inlet and exit diameters were both 6.4 cm (2.5 in), so a 59.5 cm length of 6.4 cm (2.5 in) ID PVC pipe connected the venturi to the air supply line. A 28.0 cm length of 6.4 cm (2.5 in) ID pipe was placed after the venturi upon the manufacturer recommendation that there be no flow interruptions present within at least two pipe diameters downstream. The cooling circuit then fed into the test blade, which was housed in the test section.

Design of Blade Test Section. To match the engine flow conditions around the test blade, we constructed a test section, pictured in Figure 3-4, to house three 12X scale blades. The blade layout, shown in Figure 3-5, formed two full air passages with two smaller air bleeds on the far left and right. The floor of the test section was 25.4 mm (1.0 in) thick medium density fiberboard (MDF), and the outside walls were 9.53 mm (0.375 in) thick lexan. The section ceiling was made from 12.7 mm (0.50 in) thick lexan.

The flow around the center blade, which contained the microcircuit geometry, had to be balanced to meet the midspan pressure distribution that was determined from computational predictions by Hohlfeld [2003]. Details on measuring the midspan pressure distribution are given later in this chapter. To match the predicted pressure distribution, the test section was designed with several flow adjusting components. As shown in Figure 3-5, sliding doors in the outer air bleed passages governed the amount of air that entered the passages on either side of the test blade. A rod with 28 threads per 25.4 mm (1.0 in) actuated the sliding doors, which were mounted on two more smooth rods for stability. Flexible walls of 3.18 mm (0.125 in) Plexiglas extended from the trailing edges of both outer blades. The contours of the walls were adjusted using the gear and rack mechanism shown in Figure 3-6. The block containing the gear and rack was attached to the flexible wall with a hinge joint. The gear rotated on axis with a rod that extended through the tunnel ceiling to a knob where it could be instantaneously adjusted without interfering with the flow. Schematics and parts lists of this flexible wall adjustment mechanism (FWAM) are included in Appendix A. The FWAM locations are indicated on Figure 3-5 with the white circles labeled one through five. The grouping of the FWAMs was more concentrated on the flexible wall immediately downstream of the right blade. FWAMs 1, 2, and 3 served to follow the contour of the trailing edge on the suction side of the center blade. Fine adjustments at this wall were necessary when balancing flow around the center blade to achieve the proper midspan pressure distribution. FWAMs 4 and 5 impacted the overall pressure drop of the test section. As these two opened, the tunnel experienced less flow blockage, and the inlet velocity to the test section increased. The high velocity air through the center passage created a low pressure zone that tended to pull the flexible walls together. To prevent this, the FWAMs were locked into place with set screws adding rigidity to the flexible walls where necessary.

The ability to change the tip gap is another design feature that was built into the test section. The tip gap was the gap between the tip of the center test blade and the MDF floor of the test section. This modeled the clearance between a turbine blade tip and the shroud in an actual engine. However, this clearance was only modeled in the center blade. As discussed later in this section, the outer blades served to balance the flow around the center blade. Figure 3-7 depicts the blade adjustment mechanism consisting of threaded rods and hex nuts. The base of the blade (the end opposite the tip gap) attached to a 19.1 mm (0.75 in) thick wood board. This board rested on the hex nuts, which could travel the length of three threaded rods that were anchored to the test section ceiling. The rods were 12.7 mm (0.5 in) in diameter with 20 threads per 25.4 mm (1.0 in). Figure 3-7 only shows two threaded rods for simplicity. The entire blade-baseboard assembly could traverse up and down the rods allowing the blade tip to move relative to the MDF floor.

Great care was taken to accurately set the tip gap. Aluminum blocks were machined on an end mill to the thickness of the desired tip gaps within ±0.025 mm (±0.001 in), which is 0.8% of the small tip gap height. The blade-baseboard assembly was allowed to rest on these blocks while the hex nuts were tightened into place. The blocks could then be pulled out, so that the tip gap remained. During experimentation, we began to build temporary, wooden gage blocks that set the tip gap by offsetting the distance from the baseboard to the test section ceiling, as labeled on Figure 3-7. After initially setting the tip gap inside the tunnel with the aluminum blocks, we would cut MDF blocks to the size of the distance from the baseboard to the section ceiling. This allowed us to reset the tip gap from outside the flow without turning off the tunnel. On a table saw, the wooden blocks were cut to a snug fit which is within ±0.064 mm (±0.0025 in). The total uncertainty from the aluminum block machining and the MDF block machining stacks up to 3% of the small tip gap height.

Tip Models. While the two outer blades served to shape the air flow around the center blade, the center blade was the blade of interest. There were four different tip geometries tested in this study. Figure 3-8 shows the flat tip, dirt purge cavity, dirt purge cavity with holes, and combined dirt purge-microcircuit geometries. The flat tip geometry is a plain blade with characteristics listed in Table 3-1. The coordinates of the blade profile are included in Appendix B. All blade geometries tested in this study are variations on this basic blade shape.

The dirt purge geometry is shown in greater detail in Figure 3-9. The hollow blade plenum fed coolant air through two holes that exited through the blade tip on the leading edge. This geometry is present in actual turbine blades to expel foreign particles from the blade. Centrifugal forces drive dust or dirt through the dirt purge holes preventing it from clogging smaller coolant holes located elsewhere on the blade. Sometimes, during transient engine operation, thermal expansion will cause the blade tip to rub against the shroud, so blade designers added a recess, or cavity, at the dirt purge hole exits that is intended to prevent them from being closed off. Experiments were done on a blade with the dirt purge holes and cavity as well as with the cavity only. For the case with the cavity alone, the dirt purge holes were blocked with a kneaded rubber material that was purchased at a local art supply store. The kneaded rubber created an airtight seal but could still be removed without leaving any excess rubber to obstruct the holes.

The fourth geometry studied was the blade tip containing a microcircuit channel geometry. Figure 3-10 shows the negative of the microcircuit—or the air passages without the surrounding blade material. This tip design incorporated a complex series of internal air passages that were fed by the hollow blade plenum and exited along the pressure side near the tip. The plenum supplied air to the microcircuit through ten inlet channels. After passing through the microcircuit, cool air was expelled from holes located 4.5 mm (0.18 in) from the tip. There were sixteen shaped holes, which were all 6.4 mm (0.25 in) in height and had varying widths. They are labeled in Figure 3-11 with a numbering scheme that will be used to reference these exits later in this report. The dirt purge geometry was also present in the microcircuit design and is labeled as holes 17 and 18.

The area of each microcircuit exit and dirt purge hole was calculated by Hohlfeld [2003]. Figure 3-12 charts the area of each exit as a percentage of the entire coolant flow exit area. The microcircuit exits at the leading edge had the largest exit areas followed by exit number 16 on the trailing edge. The dirt purge holes comprised 11% of the total exit area while the remaining 89% of the area was microcircuit exits. The total exit area was 13.9 cm^2 (2.16 in^2). Figure 3-13 shows the predicted coolant flow percentages through each microcircuit exit and dirt purge hole according to Praisner [2002] and Hohlfeld [2003]. Although microcircuit exits 1 through 5 each had larger exit areas, the highest coolant flows exited through the dirt purge holes. The least flow exited the midchord exits, which also have the smallest areas.

In addition to different tip geometries, two different blade materials were tested. To observe the effects of external cooling only, we constructed a blade from a foam material of a low thermal conductivity. The foam manufacturer, Stepan, provides the thermal conductivity to be $k = 0.036\text{-}0.043$ W / m K (0.25-0.30 BTU in / hr ft^2 °F). This is probably presented as a range because of material variations that can occur in the foam molding process discussed later in this section. The foam prevented heat conduction through the blade walls. Temperature measurements of this adiabatic surface would display the local fluid temperature for the tip. A second blade was built from a material of high thermal conductivity, so that heat transfer effects from internal convection in the microcircuit passages, as well as external convection effects, could be observed. Refer to Chapter 1 for a further discussion of the purpose for different blade materials. The construction processes for both blade materials is discussed in more detail below.

The adiabatic tip was built using a foam material manufactured by the Stepan Company. The Turbulence and Turbine Cooling Research Lab at the University of Texas (Bogard, 2002) provided the foam material to Virginia Tech's Experimental Computational Convection Laboratory in two liquid parts. Part A was Stepanfoam AM-9451 (polymeric diisocyanate), and part B was Stepanfoam RM-9137 (polyol). A foam material forms when a one-to-one ratio of A and B is mixed together for 30 seconds and allowed to set. In preliminary tests, the mixture immediately began expanding exothermically for about five minutes until it set leaving the completed foam material. The foam blade was created by pouring the A-B mixture into a mold and allowing the foam to expand around the desired geometry. Two components were necessary for this process: a piece to shape the air passages of the microcircuit and a piece to form the outer shape of the blade. Figure 3-14 shows the air passages and outer mold that were built on a stereo lithography (SLA) machine at Pratt & Whitney's fabrication lab. The outer mold was pulled away after the foam set, but the piece forming the air passages would become a permanent part of the final product. To prevent foam from leaking into the microcircuit air passages, a 1.6 mm (0.063 in) thick layer of SLA material closed off the microcircuit exits. The SLA layer was included as part of the microcircuit air passage piece provided by the fabrication lab and was removed with a Dremel tool after the mold process was completed. The dirt purge hole exits were plugged with kneaded rubber.

Prior to pouring the foam, the preparation of the mold was critical for good results. The expansion of the foam would cause such great pressure that, afterwards, the blade would not slide out easily. For this reason, the outer mold was cut into two pieces that could be pulled away. Figure 3-15 shows a picture of the two-part outer mold assembly. Metal shim strips filled the gap that remained after the cutting operation, and bolts were used to hold the two pieces together tightly during foam expansion. The air passage piece had tabs that could be bolted to threaded holes in the outer mold. This kept the air passages stationary during foam expansion, and later the tabs could be cut away from the final part. Also indicated on Figure 3-15 are holes that were drilled into the mold to allow excess foam to leak out. This kept the pressure in the mold from becoming so great that the SLA microcircuit passages would collapse.

The foam had a tendency to bond to the SLA material of the outer mold, so we lined all surfaces that would be exposed to foam with Teflon-coated fiberglass tape. The outer mold halves were then bolted together, and all taped surfaces were then coated with Dee-Rax, which is a resin mold release that was purchased at a local art supply store. The mold release is applied over the tape as an added measure to ensure that the foam model pulled from the mold easily after the foam set.

Before pouring the mold, it was necessary to determine the volume of foam needed to create the blade and the amount of A and B needed to create that volume. To determine the volume of foam required, we measured the volume of water that filled the assembly of our mold and air passage and determined that 1,343 cm^3 (1.42 quarts) was the volume of foam material needed to form the blade. Prior testing also indicated that 237 cm^3 (0.5 cup) of A and 237 cm^3 (0.5 cup) of B expanded into 946 cm^3 (1 quart) of foam. With this ratio we estimated the amount of A and B required and poured each into a measuring cup. An extra 25% was added to each part to ensure that the entire blade volume was formed. We vigorously mixed the two parts together for 30 seconds until the mixture had a uniform yellow color. The mixture was immediately poured into the outer mold, and the SLA model microcircuit passages were inserted and bolted down. The initial expansion of the foam took only 5 minutes, but the entire hardening process continued for several hours. Therefore, after pouring, a lid was placed on the mold, and the mold was allowed to sit for 24 hours. When the mold hardened, the two outer mold halves were knocked of with a rubber mallet leaving the final blade shown in Figure 3-16.

The second blade tested was made from an alumina oxide ceramic, which had a thermal conductivity of 1.44 W / m K (10 BTU in / hr °F ft^2). This material was known as RTC-60 and was distributed by the Cotronics Corporation. Pratt & Whitney provided the alumina blade model though some cracks had to be repaired at Virginia Tech. Broken pieces of the brittle alumina blade were reattached with a general purpose adhesive called Resbond 907GF which is also distributed by Cotronics Corporation. Material properties for RTC-60 and Resbond are included in Appendix C. This adhesive had a thermal conductivity of 0.58 W / m K (4 BTU in / hr °F ft^2). Figure 3-17 shows a picture of the alumina blade. The vertical lines are thermocouples that were installed for tests to be completed by Christophel [2003].

Both blade models were painted black to increase surface emissivities for the thermal imaging processes that are discussed later. On both blade models, we used XO-19 Flat Black spray paint manufactured by X-O Rust.

3.2 Experimental Instrumentation and Measurement Techniques

This section describes the measurement techniques and instruments used in this study. First, the methods used to verify the flow upstream of the test blade are discussed. Other subsections describe the pressure measurement and temperature measurement methodologies used. In addition, detailed descriptions of the instrumentation measuring these quantities are given wherever possible.

Flowfield Measurements. To verify that the tip was exposed to a uniform mean and highly turbulent flow, velocity profiles were measured at x/C = 0.98 upstream of the test blade. Because the apparatus used to measure velocity had to be positioned upstream of the blade inlet, the profiles were measured inside the contracting area of the combustor simulator. These profiles were measured on horizontal and vertical planes that were normal to the flow as shown in Figure 3-18. The distances of the measurement plane and dilution jets relative to the blade stagnation point are normalized by pitch, P, and true chord, C.

Measurements were made with a two component, back scatter, fiber optic, laser-Doppler velocimeter (LDV) system. A 5 W laser source provided a beam to a TSI model 9201 Colorburst separator where the beam was separated into a green and a blue beam. The beams were then routed to a probe through fiber optic cables and emitted through a 750 mm focusing lens with a beam expander. Data was processed by a TSI model IFA 755 Digital Burst Correlator which was controlled by TSI's FIND software for Windows.

For each measurement location, the z and x velocity components, w and u, were each sampled 15,000 times. Measurements were made every 25 mm (0.98 in) along most of the horizontal plane and at varying increments along the vertical plane. The probe was slightly tilted at 7.3°, so readings could be taken near the tunnel floor, which is close to the tip of the blade to be studied. Readings were taken at small increments near the tunnel floor and at larger increments as the flowfield became more uniform away from the floor. Velocities near the top of the tunnel were not measured because of the angle of the probe and were assumed inconsequential since the tip area of interest was located at the floor of the tunnel. In addition to the mean velocity measurements, root-mean-square (rms) velocities were also quantified at these locations. Turbulence levels are calculated as

$$Tu = \frac{\sqrt{\frac{1}{2}\left(u_{rms}^2 + w_{rms}^2\right)}}{u_{avg}} \qquad (3\text{-}1)$$

where u_{avg} is the velocity in the x-direction averaged over the tunnel height, and u_{rms} and w_{rms} are the streamwise (x) and cross stream (z) root-mean-squares of the velocity fluctuations, respectively.

To determine what dilution flow settings were required to get turbulence levels of nominally 10%, velocity and turbulence profiles were measured at four different dilution mass flow settings, which were expressed as a percentage of the mass flow exiting the main passage of the combustor simulator. The mass flow of the combustor simulator was calculated from dynamic pressure measurements made at seven locations across the midspan of the exit. These profiles were acquired without any thermal conditioning because Colban [2002] showed that total pressure profiles in this region are nearly unaffected by the density variation from heating.

Figure 3-19 shows the results from the vertical profile readings The LDV measurements show velocities close the floor were most uniform for the cases with 4.3% and 5.6% of the combustor exit mass flow. Turbulence levels of about 10% best simulate actual combustor turbulence before the turbine, and the 4.3% and 5.6% cases both satisfied this requirement. Because more dilution flow would reduce the freestream temperature and, thus, reduce the overall resolution of the thermal field measurements, we investigated the 4.3% dilution flow setting.

The horizontal plane results, shown in Figure 3-20, suggest that a symmetric velocity profile is present for this case. The largest variation in velocity across the horizontal plane was 9% of the mean. This suggests that the individual effects of the dilution jets have are mixing out on the horizontal direction. Figure 3-20 also shows the cross-stream component of the flow normalized by the averaged x-velocity. The turbulence levels are based on streamwise fluctuations, Tu_u, and cross-stream fluctuations, Tu_w where

$$Tu_u = \frac{u_{rms}}{u_{avg}} \tag{3-2}$$

and

$$Tu_w = \frac{w_{rms}}{u_{avg}} \tag{3-3}$$

Figure 3-21 shows vertical profiles for these same values at the 4.3% dilution flow. At one chord upstream of the test blade, we estimate a boundary layer thickness of 22 mm (0.87 in) or 4.0% of the blade span. This boundary layer is more than twice the size of the large tip gap, which is 9 mm (0.35 in) or 1.63% of the blade span. We decided to run all tests in this report with a dilution flow at 4.3% because it provided a uniform vertical velocity profile, horizontally symmetric flow, and turbulence levels near 10%. The momentum flux ratio between the dilution and the freestream at the 4.3% dilution flow setting is 8.4. The momentum flux ratio is defined as

$$I = \frac{\rho_j U_j^2}{\rho_\infty U_\infty^2} \tag{3-4}$$

where ρ_j is the density of the air exiting the dilution hole, U_j is the velocity of the dilution air, ρ_∞ is the density of the mainstream air in the combustor, and U_∞ is the velocity of the mainstream air.

As a continual check of the uniformity of the test section inlet velocity, dynamic pressure measurements were made along the combustor simulator exit with a pitot probe prior to all data collection. The pitot probe was inserted into the flow through seven ports evenly spaced across the 112.0 cm width of the tunnel. The pressure reading was measured on a 0-125 Pa (0-0.5 inH2O) transducer and then converted to a velocity based on the inlet area and the density of air. Figure 3-22 shows the pitot probe location in the z-x plane. The pitot probe extended about 21.6 cm into the tunnel, which was about 39% of the full height of the combustor simulator exit measured from the top. Figure 3-23 shows a sample inlet velocity profile for one of the cases. The local and mean velocities are plotted against the measurement location in the y-direction. Inlet velocities were typically within 5% of the mean. If this were not the case, adjustments were made as necessary to the outer flow gates and FWAM's, so that conditions at the tip region were consistent for all cases.

Pressure Measurements. To better understand the leakage flow across the tip gap, static pressure readings were made along the shroud below the test blade with an array of static pressure taps. Each static pressure tap was installed across the shroud in the configuration shown in Figure 3-24. The location and quantity of taps was determined using computational predictions of the pressure distribution along the shroud with a flat tip. Pressure taps were grouped more tightly where high pressure gradients were predicted. Figure 3-25 shows 112 tap locations overlaying the predicted pressure distribution. Also shown are ten more taps that were installed after our first tests to further improve the resolution in areas with high pressure gradients. The locations of all 122 taps are documented in Appendix D.

Pressure measurements were also made at the midspan on the test blade to verify that the flow was periodic about the center blade. Sixteen static pressure taps were placed along the center blade at 36% of the blade span above the tip in the same configuration as in Figure 3-24. The locations of the midspan static pressure taps are diagramed in Figure 3-26, and their locations are listed in Appendix D. Pressure readings from these taps were used to verify that the pressure distribution around the center blade agreed with the distribution computationally predicted by Hohlfeld [2003]. Typically, the adjustable components of the test section could be set to achieve good agreement with computational predictions as shown in the sample midspan pressure distributions in Figure 3-27. The midspan pressure distributions for the highest and lowest blowing ratios are shown for two tip gaps. Values for C_p are plotted against the normalized surface distance along the blade from stagnation, s/s_{max}. The pressure side of the blade ranges from $s/s_{max} = -1$ to 0, and the suction side ranges from $s/s_{max} = 0$ to 1. For all cases the experimental midspan pressures match closely to the predicted values along the pressure side and around the stagnation location. However, with the large tip gap the experimental C_p values are higher (smaller negative values) on the suction side than the predicted values. This is likely due to the fact that a periodic boundary condition does not exist at the flexible wall near the suction side of the blade as it does in the computer model. Therefore, the greater leakage flow through the large tip gap contributed to lower pressures on the suction side. The test section flow settings were adjusted to improve agreement with predicted values, but perfect agreement could not always be achieved due to the limited the range of motion of the FWAM's and bleed gates.

The midspan and shroud pressure taps were routed to a Scanivalve wafer through 1.6 mm (0.063 in) ID vinyl tubing. This tubing was distributed by the Scanivalve Corporation as part number VINL-063. The Scanivalve wafer shown in Figure 3-28 allows different pressure channels to be read at the turn of a knob. Six Scanivalve wafers with each having 24 different ports served as junctions to the transducer box. The transducer box, shown in Figure 3-29, housed eight transducers that measured pressure differences and expressed them as voltage on a 0 - 5 V range. Table 3-2 lists the pressure transducers used in this study along with their ranges. All static pressures in this study were measured relative to atmospheric pressure and then readjusted relative to the stagnation pressure of the center blade.

The voltage signal from the transducers were processed by a National Instruments SCXI-1100 data acquisition board, which was set to read a 0 – 10 V analog input, and then fed to a computer A/D board. Digital signals from the 12-bit A/D board were then processed and displayed in National Instrument's LABVIEW software. LABVIEW was set to sample 5,000 points at a rate of 1000 scans per second with a gain setting of 1.

Temperature Measurements. Surface temperatures on the tip of the blade were measured with the Inframetrics model 760 infrared camera pictured in Figure 3-30. To reduce levels of uncertainty, the camera was set to record images that were averages of sixteen temperature readings. The uncertainties in the infrared camera measurements are discussed in Section 3.4. The camera made tip temperature measurements through a window that passed infrared wavelengths. This window had to be part of the shroud and, thus, be large enough to image the entire tip surface. However, many infrared transmissive materials are so expensive that the cost of such a large window rendered this option infeasible.

Potassium Bromide (KBr) crystal was a more affordable material that was manufactured by Thermo Hilger Crystals. When polished, this particular crystal was 90% transmissive over wavelengths of light from 0.4 to 20 μm. This offered excellent transmission for our longwave camera, which transmitted infrared light between wavelengths of 8 to 12 μm. However, KBr is water soluble and very brittle. Although great care was taken to expose the window to as little moisture as possible, our window began developing cracks because of the thermal expansion during testing, and it eventually broke.

A second purchase was made that was less likely to break but offered less transmissivity. The REFLEX Analytical Corporation manufactured a Zinc Selenide (ZnSe) window which passed the 8 to 12 μm wavelength rage at about 70% transmissivity. We were able to purchase two 10 mm (0.39 in) thick, 15.2 cm x 15.2 cm (6 in x 6 in) windows that together could cover half of the blade. The two ZnSe windows were placed inside an aluminum frame to protect them from the stresses caused by the thermal expansion of the lexan shroud during tests.

In order for the camera to image the tip surface, the MDF floor was replaced with a 12.7 mm (0.5 in) thick lexan floor that had a 59.1 cm (23.25 in) x 17.1 cm (6.75 in) rectangular area cut out below the test blade. This slot housed the infrared window and frame. It was not possible to purchase a window large enough to view the entire blade, so half of the blade was imaged through the ZnSe windows in the slot while the other half of the slot was covered and sealed with a lexan lid. Then, the window was moved into position to image the other half of the blade. The tip gap had to be increased to reposition the window, so the wind tunnel velocity was brought down and the test blade was moved. Once the window and lexan lid were in place, the tip gap and wind tunnel conditions were reset. The second half of the blade was not imaged until the tunnel conditions indicated a steady state, which is described in Section 3.3. Figure 3-31 illustrates the window positioning scheme in which the frame and insert are set into two configurations to allow the entire tip surface to be imaged. The frame and lid rested on a lip around the slot in the lexan shroud. A small screw at each corner of the frame fixed it in place and prevented it from being pulled up from the lip by the low pressures inside the tunnel. Two metal blocks weighing 22.2 N (5 lbs) each were hooked to the handles of the insert to keep it in place. Special care was taken to insure that the windows, aluminum frame, and lid were flush along the tunnel floor, so that no major flow disruptions arose from discontinuities along the shroud. Detailed schematics of the lexan shroud, lexan lid, and aluminum window frame are included in Appendix E.

The camera was positioned under the window as depicted in Figure 3-32. The camera viewing angles of 20° and 15° to formed a rectangular viewing area with side lengths determined by

$$a = 2 \times L \times \sin 10^\circ \qquad (3\text{-}5)$$

$$b = 2 \times L \times \sin 7.5^\circ \qquad (3\text{-}6)$$

where a and b are the lengths of the viewing area sides and L is the distance from the camera lens to the tip surface. The camera lens was positioned 54.6 cm (21.5 in) from the tip, so that the resultant 19.0 cm x 14.3 cm (7.49 in x 5.63 in) viewing area covered at least a fourth of the blade. The camera recorded this viewing area to disk as a 255 x 206 pixel image (a temperature value is designated to each pixel). This correlates to an image resolution of 194 pixels per cm^2. In other words, each pixel represents a 0.05 x 0.05 mm (0.002 in x 0.002 in) area. The temperature value assigned to each pixel is averaged over a 3.7 mm (0.15 in) diameter area.

The infrared camera captured temperature data at the four different portions of the blade. These images would later be assembled to provide a complete thermal image of the tip. Markers with known positions relative to the dirt purge holes were inserted into the blade tip making it possible to assemble the four images correctly. The markers were 1.6 mm (0.063 in) diameter brass tubes with a chamfer on the 0.8 mm (0.031 in) inner diameter, which reflected light in such a way that they were easily distinguished on the infrared image. Figure 3-33 presents an unprocessed image with markers.

These images were calibrated with thermocouples embedded in the tip surface of the blade. The foam tip had three calibration thermocouples, two on the leading edge and one on the trailing edge half of the blade. There were eight calibration thermocouples placed on the alumina tip, so that there were two thermocouples in each of the four images. Whenever possible, one thermocouple was placed in a cooler region and the other in a warmer region. Figure 3-34 shows the marker locations and thermocouple locations for the foam and alumina tips. The area around the blade that can be viewed through the ZnSe windows is marked with a dashed line. There is some overlap at the midchord between window configurations to ensure that the entire blade is imaged.

For both the foam and alumina tips, type E thermocouples were used to calibrate the camera images, but different thermocouple beads had to be used for the different materials. Spherical thermocouple beads of diameter between 0.8 mm to 1.0 mm (0.031 in to 0.040 in) were slightly embedded into the surface of the foam tip. With an adiabatic assumption, the temperature of the tip surface is the temperature of the air close to the tip surface as well as the temperature of the foam below the tip surface. If the thermocouple slightly protruded out into the tip leakage flow or was slightly more embedded in the foam, it still represented the tip surface temperature accurately. This was not true for the alumina tip case in which heat was conducted from the blade material near the thermocouple. To insure that the thermocouple was located at the tip surface, flat thermocouple strips were constructed with 0.04 mm (0.0015 in) thick ribbons of constantan and chromel (the wire material used in type E thermocouples). The ribbons were purchased from Nanmac Corporation under part number 655 for the chromel and part number 656 for constantan. Figure 3-35 depicts the layout of a flat thermocouple which is soldered to type E thermocouple wire. The chromel and constantan ribbons are overlapped and spot welded with a small arc welder.

The thermocouples were used to calibrate images recorded by the infrared camera. Once the images were recorded to disk, they were calibrated on a software package released by FLIR Systems called ThermaCAM Researcher 2001. The background temperature, T_b, and surface emissivity, ε, were adjusted on this software until the images agreed with the calibration thermocouples. Both the foam and alumina blade tips were painted black, so they could be near perfect emitters. Instead, emissivity was 0.82 for the foam tip and 0.60 for the alumina tip. The emissivity was held for all images, and the background temperature was adjusted until temperatures within the area around the thermocouple in the image matched the reported temperature. The foam tip had two calibration thermocouples on the leading edge half of the blade and one on the trailing edge half. The two front half images were calibrated to the two thermocouples on the front edge while the two images of the back half of the blade were calibrated to the trailing edge thermocouple. Therefore, one background temperature was assigned to the front images and another was assigned to the back images. The alumina tip had two thermocouples in each image, so each image was designated a different background temperature. Because of uncertainties in the thermocouples, it was not always possible to match the image to the thermocouples exactly when there was more than one thermocouple in the image. The background temperature was considered satisfactory when both thermocouples were matched within 1.0°C, based on uncertainties in the thermocouples and the camera. Once calibrated, the four images were exported to MATLAB as a 255 x 206 matrix of temperature values. An in-house MATLAB code written by Christophel [2003] assembled the images based on the marker locations, isolated all data on the tip, converted the temperatures to dimensionless effectiveness values, and output contour plots of these effectiveness values. The data from these contours were then plotted using Tecplot software.

Other temperatures recorded in this study were the coolant temperature and the freestream temperature. The coolant temperature was measured by two thermocouples inside the microcircuit plenum. One of these was placed near the dirt purge inlets to indicate possible ingestion of the freestream flow. For the cases with blowing from the microcircuit and dirt purge holes, the plenum thermocouples were typically within 1°C of each other, and the coolant temperature was considered to be an average of the temperatures reported by the plenum thermocouples. With dirt purge blowing alone, the thermocouple located near the dirt purge inlets consistently read lower than the other plenum thermocouple. For these cases the coolant temperature was considered to be the temperature reported by the thermocouple near the dirt purge inlets. The freestream temperature was measured by two thermocouples on the stagnation point at different spanwise locations of the blade. One thermocouple was placed near the microcircuit exits at about 3 microcircuit channel heights from the tip, and the other thermocouple was placed closer to midspan at 30 microcircuit exit heights from the tip.

3.3 Testing Procedures and Repeatability

This section describes the tunnel settings used during temperature measurements on the tip and pressure measurements on the shroud. It also reports results from repeatability tests for these measurements.

Coolant Flow. The coolant air to the tip was varied at four blowing ratios for both the dirt purge only and the dirt purge with microcircuit cases. The flowrates measured on the venturi tube are listed in Table 3-3 for each case. As previously discussed, the coolant was supplied by a pressurized tank at the Virginia Tech power plant and a tank in the Aerospace Department. Because the tank at the power plant was a dependable air supply, it was used to supply coolant as often as possible. For blowing ratios that were lower than 1.5%, all of the coolant was supplied by this tank. However, cases with blowing ratios of 1.5% and 2.0% required supply air from both tanks. In these cases, the valve from the power plant tank was fully opened, and supplementary air was bled off of the second tank in the Aerospace Department. It was necessary to recharge the second tank every so often because it was not continuously pressurized. Typically, if the second tank was charged up to 300 psi and then bled at the 2.0% blowing ratio, the tank pressure would drop about 50 psi over an hour. By opening the valve slightly every ten minutes, the flowrate to the blade plenum could easily be maintained within ±0.0006 kg/s (±1.0%). Nevertheless, the second tank would require recharging ever two hours.

Steady State Settings. Before tip temperature measurements could be taken, the wind tunnel would have to reach a steady state. Table 3-4 summarizes the thermal conditioning settings used in this study. After the tunnel conditions were set, the temperatures of the freestream, plenum, blade tip, and chiller reservoir were recorded every fifteen minutes. The tunnel was considered to be at steady state once temperatures were constant and showed no increasing or decreasing trends over several fifteen minute intervals. The freestream temperature and cooling temperatures were the strongest indicators of steady state and were closely monitored. From initial startup, the tunnel reached steady state in four to five hours. When the window positions are changed the 50 hp fan speed is reduced to 20 Hz for three to four minutes. When the tunnel speed is returned to 59 Hz, it took one hour to return to steady state. Depending on conditions surrounding the wind tunnel, the steady state cooling temperature and freestream temperature were 28-30°C and 50-52°C, respectively. These temperatures typically gave a ΔT of about 22°C, which governs the uncertainty in the effectiveness results. This uncertainty is further discussed in Section 3.4.

Repeatability. Tests demonstrated reasonably good agreement between results from tests run on different days with the same flow and tip settings. Figure 3-36 shows adiabatic effectiveness results from two separate cases with a large tip gap and a 1.0% blowing ratio from the microcircuit and dirt purge holes. As explained later in Chapter 4, lateral averages of effectiveness can be calculated to better quantify the contours. Figure 3-37 shows the lateral averages plotted against the normalized axial chord. The largest disagreement occurs along the trailing edge in a hot region between exits 15 and 16. This difference can be attributed partly to the small width of the blade in this area, which causes a slight disagreement in contours to be weighted more heavily to the average at that axial location. Between the two cases, the average difference in laterally averaged adiabatic effectiveness along the axial chord was 0.007. Tests for the shroud pressure distribution also indicated good repeatability. Figure 3-38 shows repeatability for a large tip gap on a flat tip. Both cases show C_p values of between -15 and -16 on the shroud near the midchord.

3.4 Uncertainty Analysis

Overall uncertainties were calculated for high and low η, ϕ, and C_p values according to the partial derivative method described in Moffat [1988]. The total uncertainty of any measurement was calculated as the root of the sum of the squares of the precision uncertainty and the bias uncertainty.

The precision uncertainty for measurements made with the infrared camera was determined through an analysis of five calibrated images taken in succession on one portion of the tip at constant conditions. Typically, it took one to two minutes for the camera to record the five images. Each image is an average of 16 temperature measurements. One averaged reading on each image was chosen from a region of high temperature gradient so that a conservative estimate of uncertainty could be made. The precision uncertainty is calculated to be 0.313°C, which is the standard deviation of the five readings corrected for a 95% confidence interval. This quantification of the precision uncertainty does not take into account that reported effectiveness values are actually averages of five images, which were each averaged over sixteen readings (a total of 80 temperature readings) and, thus, is an overestimation of the actual precision uncertainty. The camera manufacturer reported the bias uncertainty as 2.0% of the full scale. The largest scale used in this study was 20°C though some images could be captured on a 10°C range. The thermocouples measuring the freestream and coolant temperatures were reported by the manufacturer to read within ± 0.2°C. The total uncertainties for all reported values are summarized in Table 3-5.

Because η and ϕ were measured and calculated in the same way, their uncertainties are interchangeable. Large effectiveness values were reported within 0.026

(2.6%) while an effectiveness value of 0.20 carried an uncertainty of 0.025 (12.5%).

C_p values on the shroud and midspan were based on uncertainties of the transducers and data acquisition system. The precision uncertainty for readings taken on transducers was based on the standard deviation of five pressure measurements. The precision uncertainty was calculated for several sampling rates and sampling sizes to optimize a sampling scheme for testing. Based on an acceptable uncertainty and sampling time, the pressure transducers were sampled 5,000 times over a period of 5 seconds. Bias uncertainties varied for different pressure transducers but were typically 1% of the transducer's full scale. The largest transducer scale used was 0-1245 Pa (0-5 inH2O) and had overall uncertainties of 1.29 (7.4%) for high values and 1.33 (7.5%) for low values. Some pressure readings on the shroud were too large to measure with our transducers, so a 0-4982 Pa (0-20 inH2O) manometer was used. The overall uncertainties for these measurements are also reported on Table 3-5. The overall uncertainties were larger than the uncertainties for transducer measurements. However, as a percentage of the reading, the uncertainties were nearly identical. Uncertainty calculations are presented in detail in Appendix F.

Table 3-1 Blade Parameters

Blade Parameter	Symbol	Value
Scaling Factor	X_t / X_e	12
Inlet Angle	θ	16.5°
Blade Angle	ϕ	50°
Axial Chord	B_X	0.345 m
True Chord	C	0.534 m
Pitch	P	0.430 m
Span	S	0.552 m
Large Tip Gap Height		1.63% of span
Small Tip Gap Height		0.54% of span

Table 3-2 Pressure Transducers

Transducer Number	Manufacturer	Serial Number	Range (Pa)	Range (inH2O)
1	Omega	605181167	0-125	0-0.50
2	Setra	17536379	0-1245	0-5.0
3	Setra	1753678	0-623	0-2.5
4	Setra	1083664	0-125	0-0.5
5	Setra	1258460	0-62	0-0.25
6	Setra	1185967	0-1245	0-5.0
7	Setra	1185966	0-1245	0-5.0
8	Omega	60518721	0-498	0-2.0

Table 3-3 Coolant Flows

Case	Blowing	Coolant Flowrate (kg/s)
Dirt Purge Only	0.10%	0.0031
	0.19%	0.0059
	0.29%	0.0090
	0.38%	0.0117
Dirt Purge and Microcircuit	0.50%	0.0153
	1.00%	0.0305
	1.50%	0.0452
	2.00%	0.0592

Table 3-4 Steady State Flow Settings

Flow setting	Method of Measurement	Units	Value
Fan Frequency	Digital readout of frequency device	Hz	59
Primary Heat Exchanger	Flowmeter	gpm (m^3/hr)	10 (2.27)
Secondary Heat Exchangers	Flowmeter	gpm	0*
Chiller Reservoir Temperature	Digital readout on chiller control panel	°F (°C)	54 (12)**
Heater Bank 1	Digital readout on control panel	% of full power	68
Heater Bank 2	Digital readout on control panel	% of full power	68
Heater Bank 3	Digital readout on control panel	% of full power	68
Dilution Flow	Pitot probe at dilution exit	inH2O (Pa)	0.725 (181)
FWAM 1	Visual Inspection	% of full range of motion	40% open
FWAM 2	Visual Inspection	% of full range of motion	60% open
FWAM 3	Visual Inspection	% of full range of motion	80% open
FWAM 4	Visual Inspection	% of full range of motion	100% open
FWAM 5	Visual Inspection	% of full range of motion	100% open
Inner Bleed Gate	Measured with ruler	inches (cm) of gate exposed to	9.25 (23.5)
Outer Bleed Gate	Measured with ruler	inches (cm) of gate exposed to flow	3.375 (8.57)

* Secondary air was brought in from sources outside of the tunnel for most tests. The secondary heat exchangers were used for cases with only the dirt purge blowing and were set to 7gpm (1.59 m^3 / hr).

** The chiller was actually set to maintain a reservoir temperature of 45°F (the minimum temperature that can be set) to ensure that the compressor did not cycle on and off. The value presented in the table is the reservoir temperature that the chiller was able to maintain at steady conditions.

Table 3-5 Uncertainties of Reported Values

Variable	**Value**	**Total Uncertainty**
η, ϕ	1.00	0.024 **(2.4%)**
η, ϕ	0.20	0.027 **(13.3%)**
C_p w/ transducer	17.3	1.29 **(7.4%)**
C_p w/ transducer	-17.8	1.33 **(7.5%)**
C_p w/ manometer	45.7	3.39 **(7.4%)**
C_p w/ manometer	-55.7	4.18 **(7.5%)**

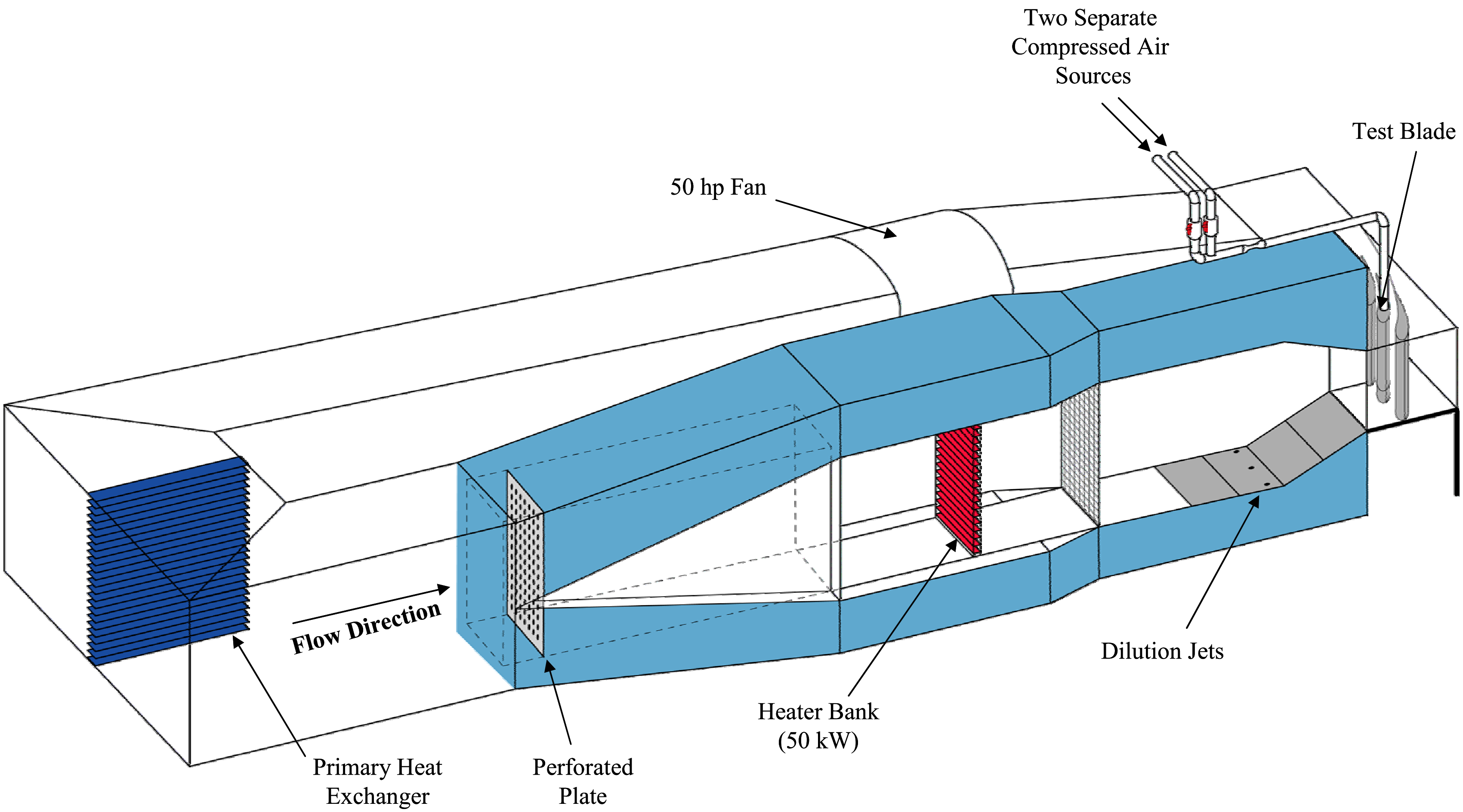

Figure 3-1 Tests were conducted in a low speed wind tunnel. The shaded area is the combustor simulator.

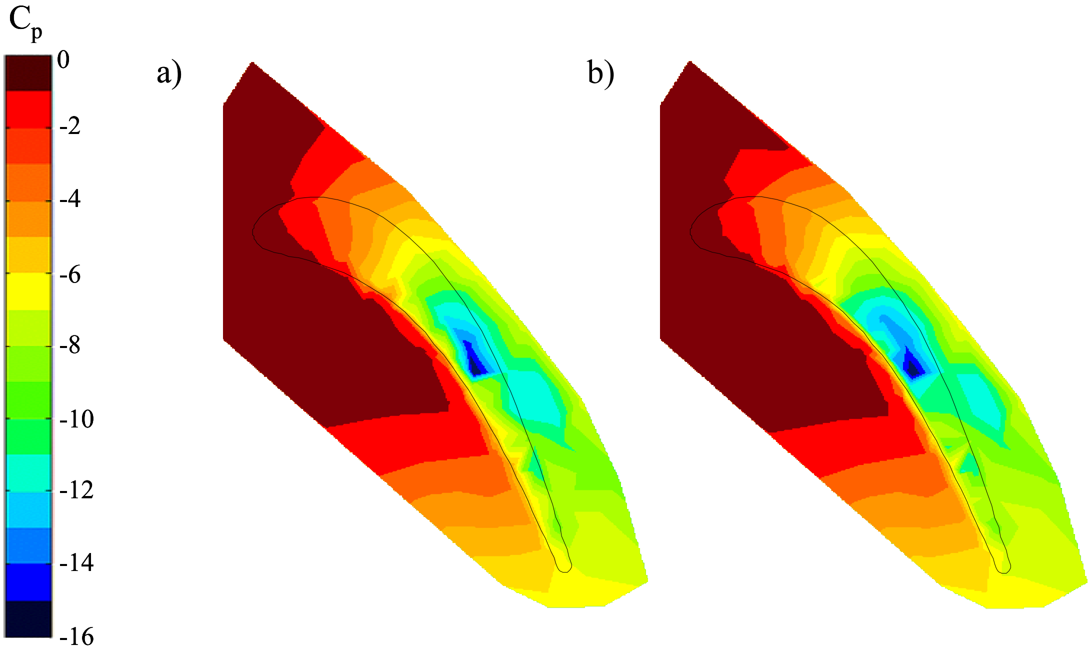

Figure 3-2 Static pressure distributions on the shroud a) without a trip wire and b) with a trip wire.

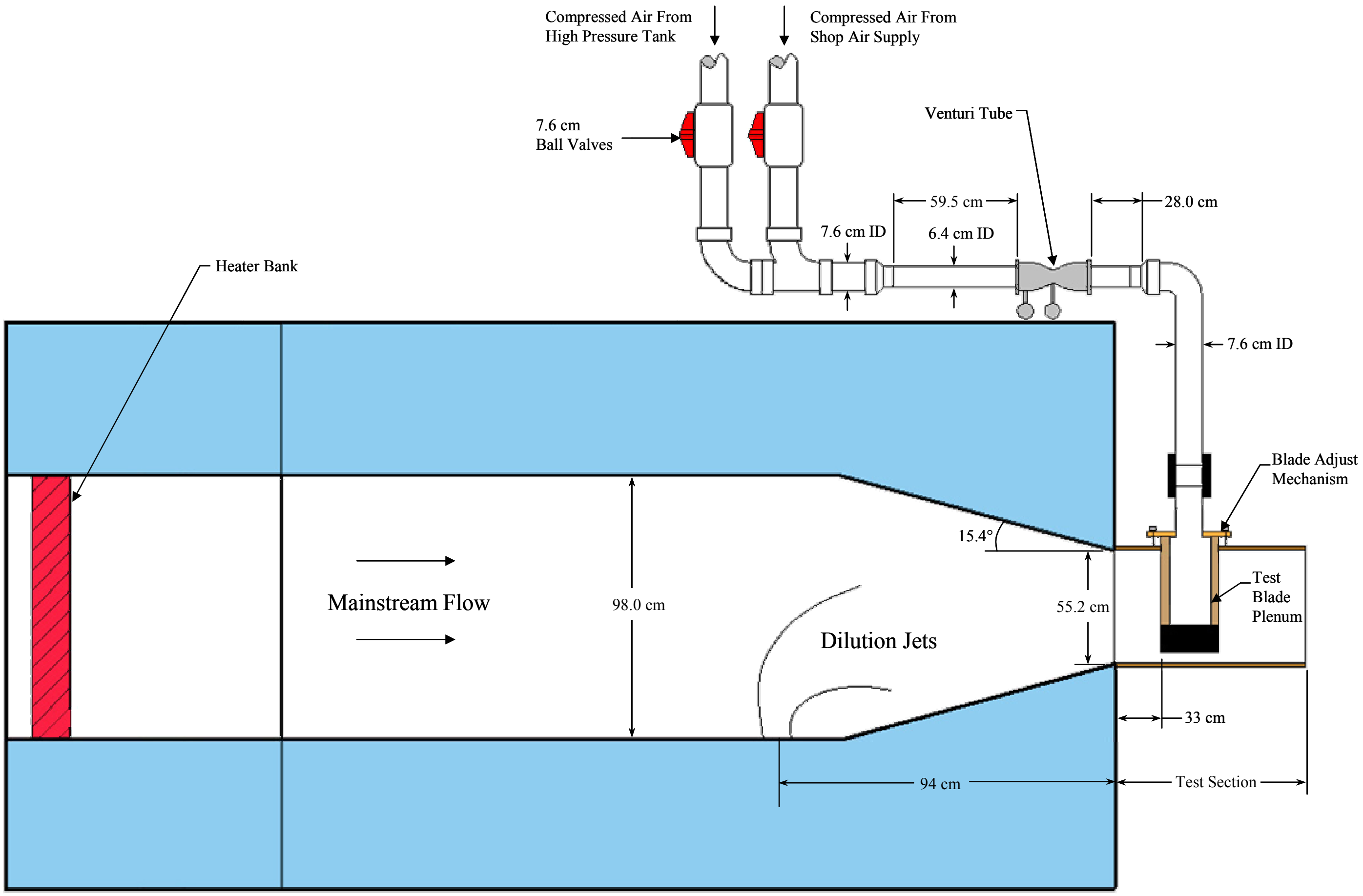

Figure 3-3 Schematic of route for secondary air to the microcircuit.

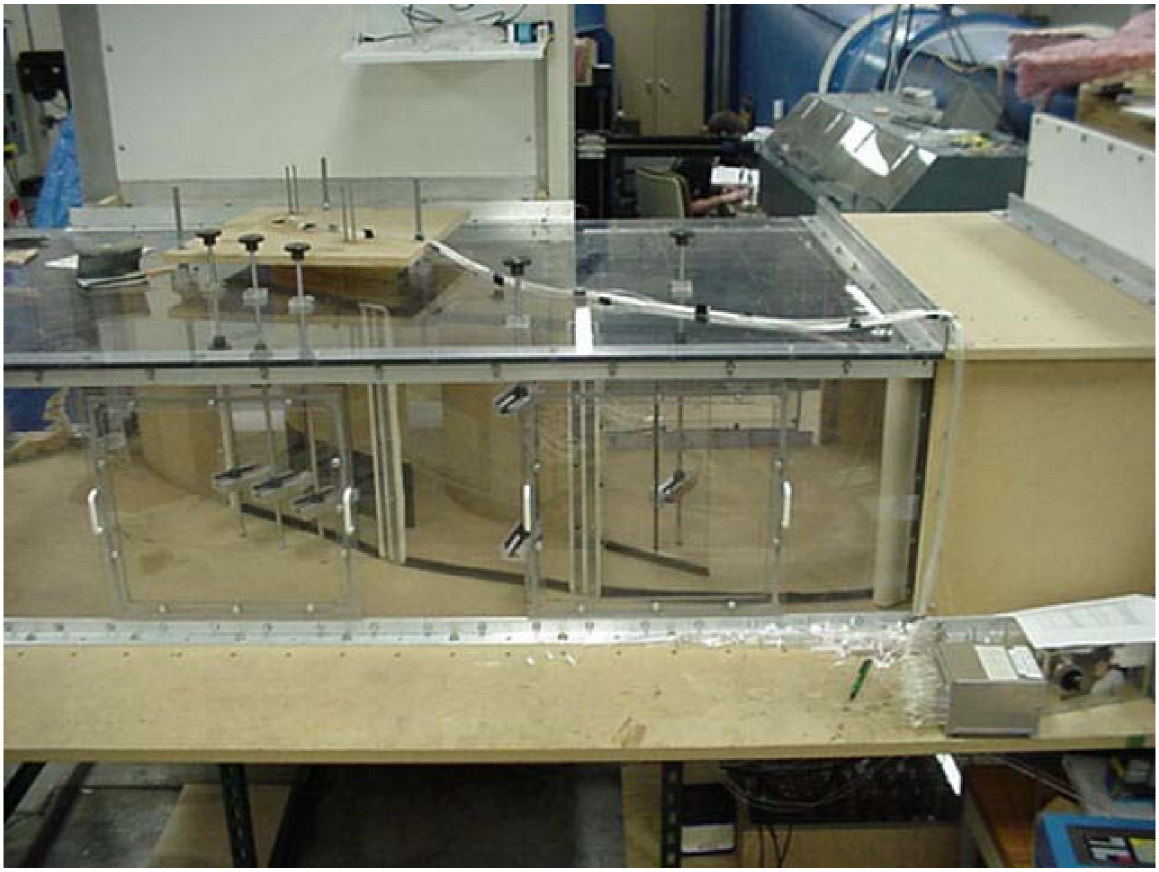

Figure 3-4 Picture of the completed test section.

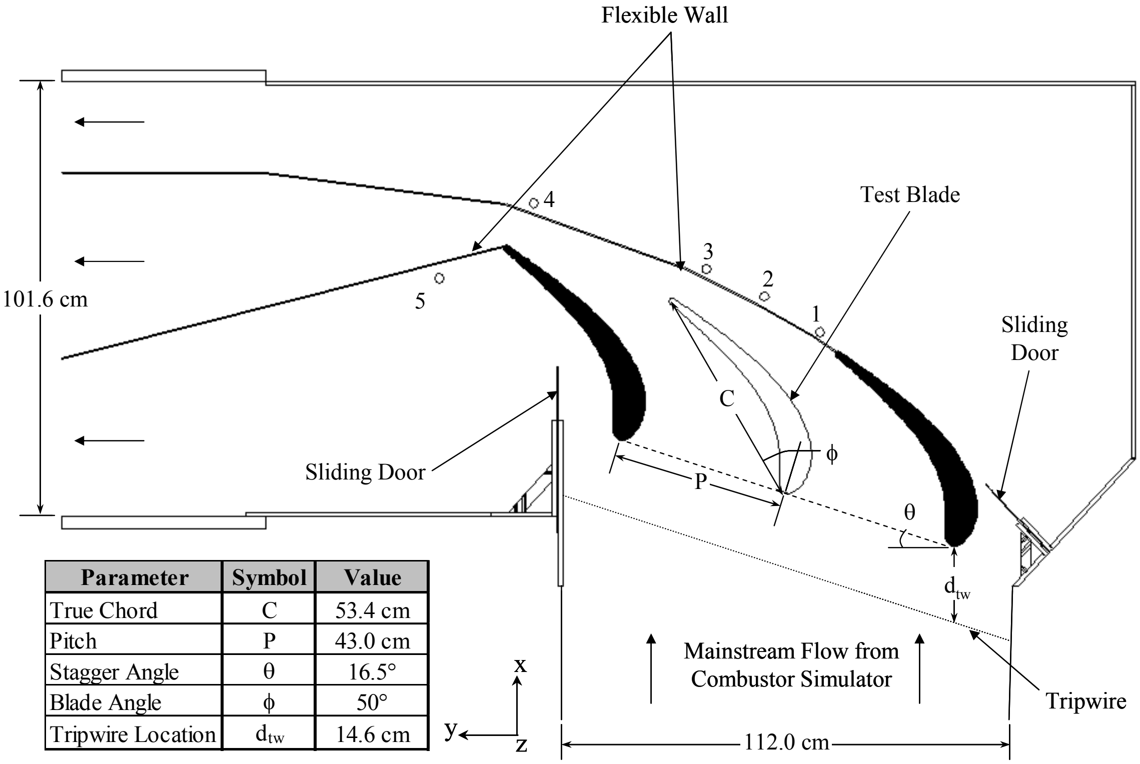

Parameter	Symbol	Value
True Chord	C	53.4 cm
Pitch	P	43.0 cm
Stagger Angle	θ	16.5°
Blade Angle	ϕ	50°
Tripwire Location	d_{tw}	14.6 cm

Figure 3-5 The test section for the wind tunnel houses three blades, which form two full passages. Flexible walls allow the flow to be adjusted around the test blade in the center.

Figure 3-6 Flexible wall adjustment mechanism (FWAM).

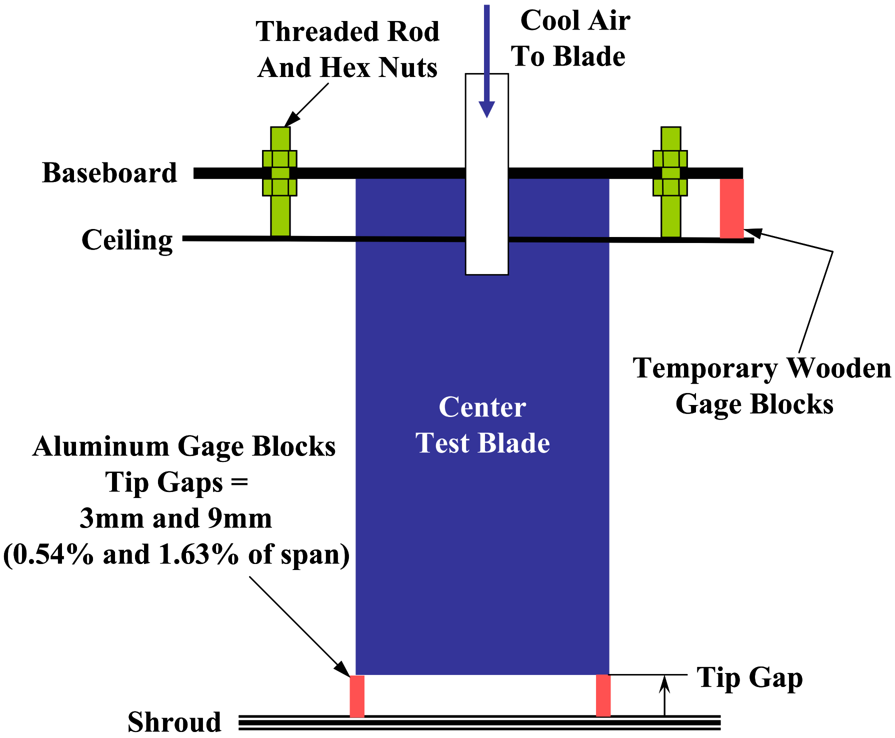

Figure 3-7 Setting the tip gap. The center blade and baseboard assembly traversed vertically along the threaded rods while gage blocks set the distance for the proper tip gap.

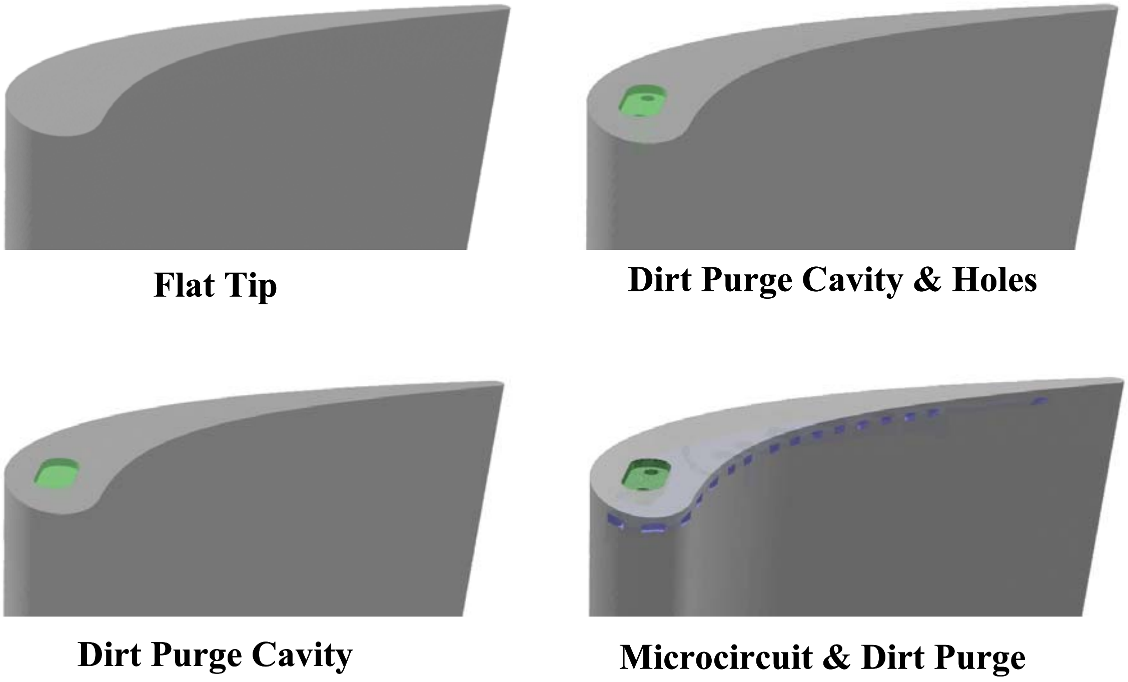

Figure 3-8 Four different tip geometries (Hohlfeld, 2003).

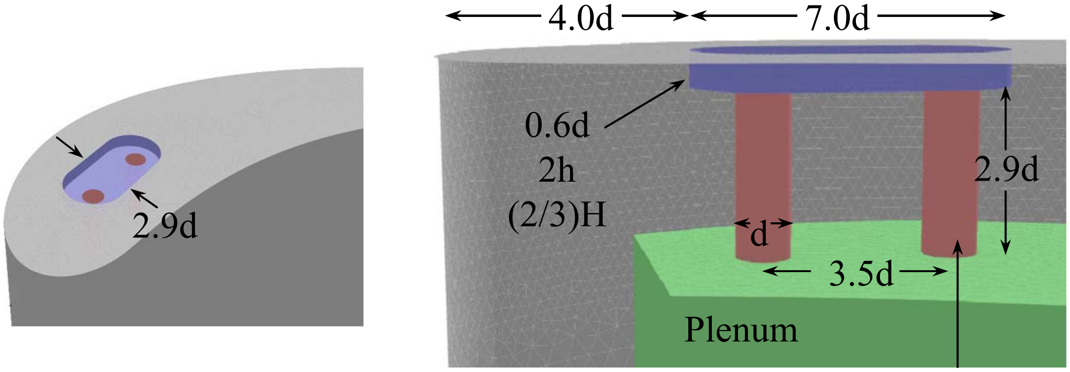

Parameter	Symbol	Value
Dirt Purge Hole Diameter	d	10 mm (0.394 in)
Large Tip Gap Height		9 mm (0.354 in)
Small Tip Gap Height		3 mm (0.118 in)

Figure 3-9 This three-dimensional depiction of the test blade shows the inner components of the dirt purge geometry that was tested in the wind tunnel (Hohlfeld, 2003).

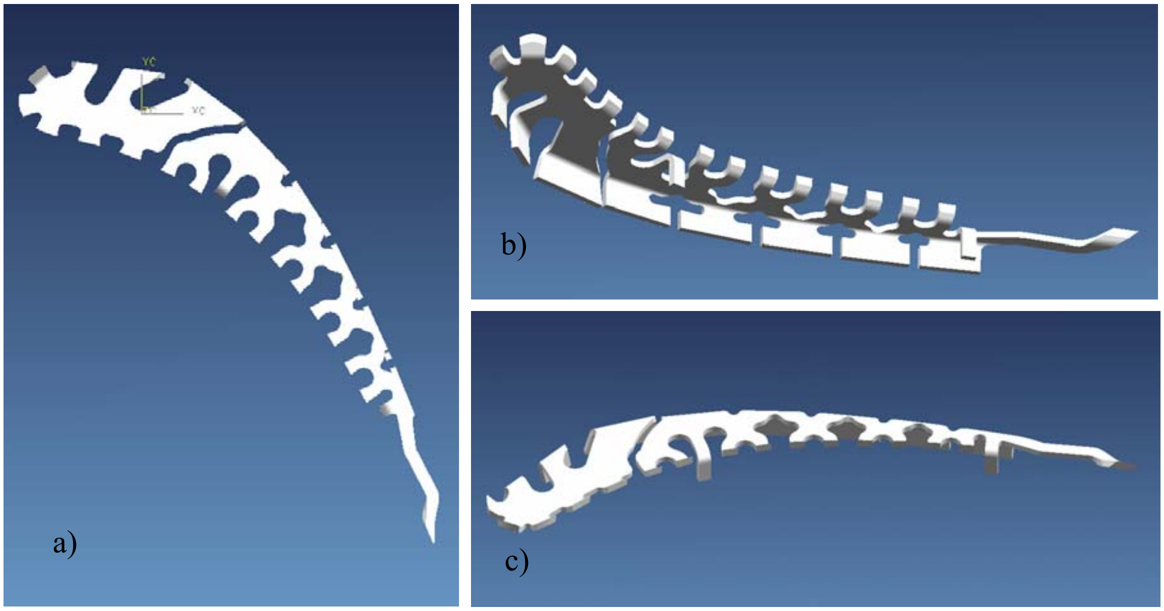

Figure 3-10 Negative image of the tip microcircuit geometry from a top view and two isometric views looking at the side from above and below the microcircuit (Hohlfeld, 2003).

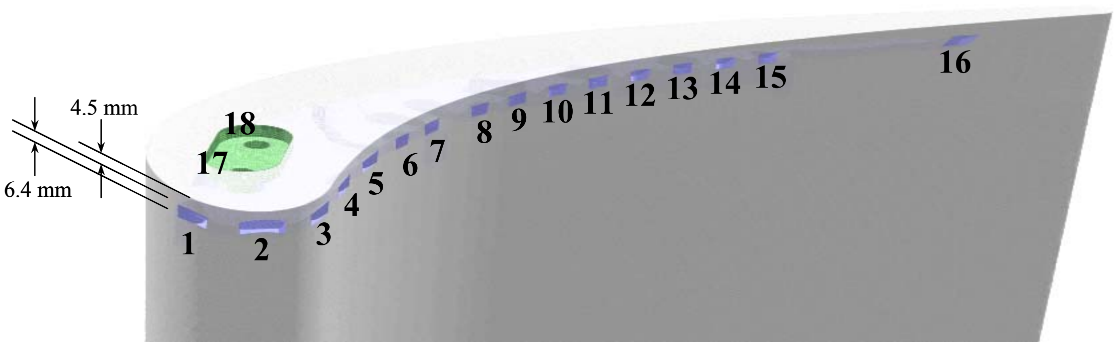

Figure 3-11 Tip microcircuit numbering scheme for referencing various flow ducts (Hohlfeld, 2003).

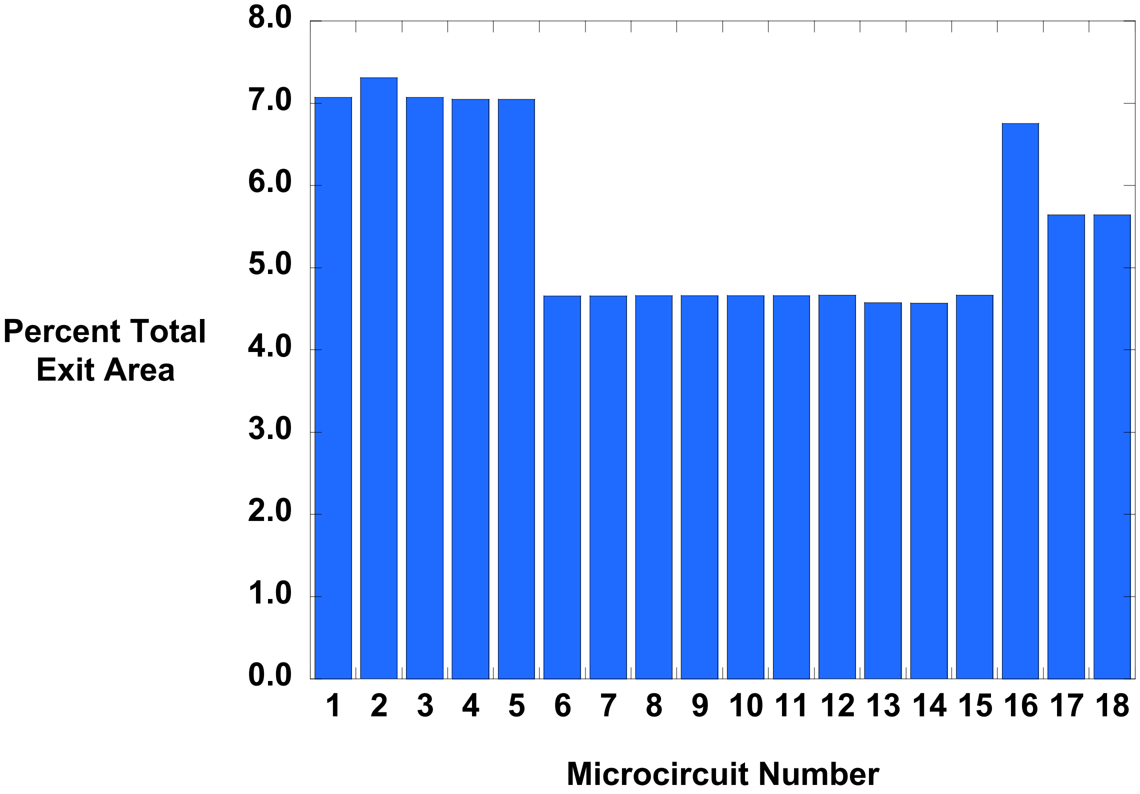

Figure 3-12 Exit area of each tip microcircuit and dirt purge hole when compared to the entire coolant flow area (Hohlfeld, 2003).

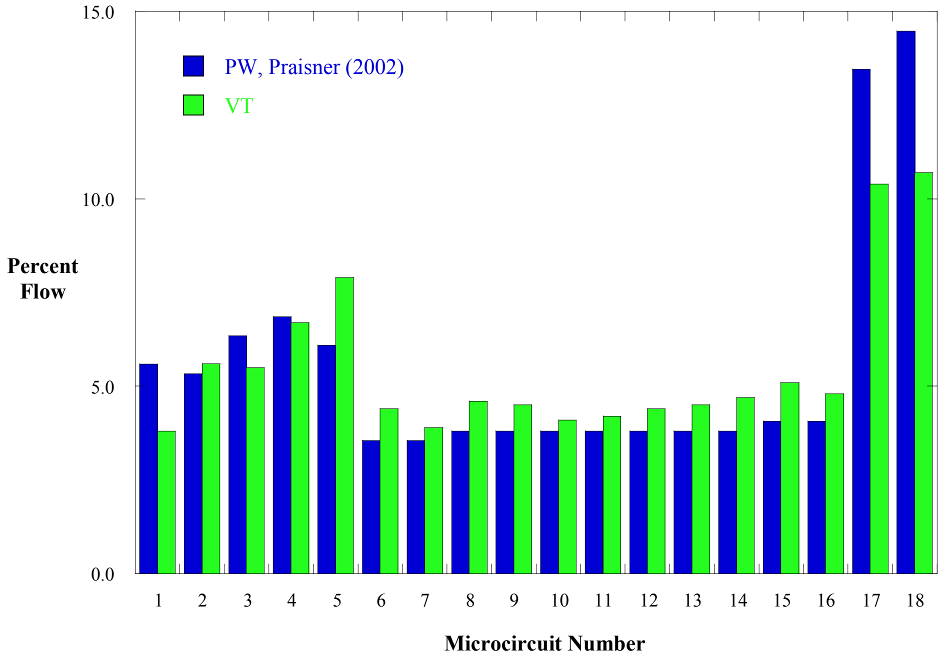

Figure 3-13 Comparison of flow distribution within the microcircuit. Numbers 1-16 represent the microcircuit holes with 17 and 18 the dirt purge holes (Hohlfeld, 2003).

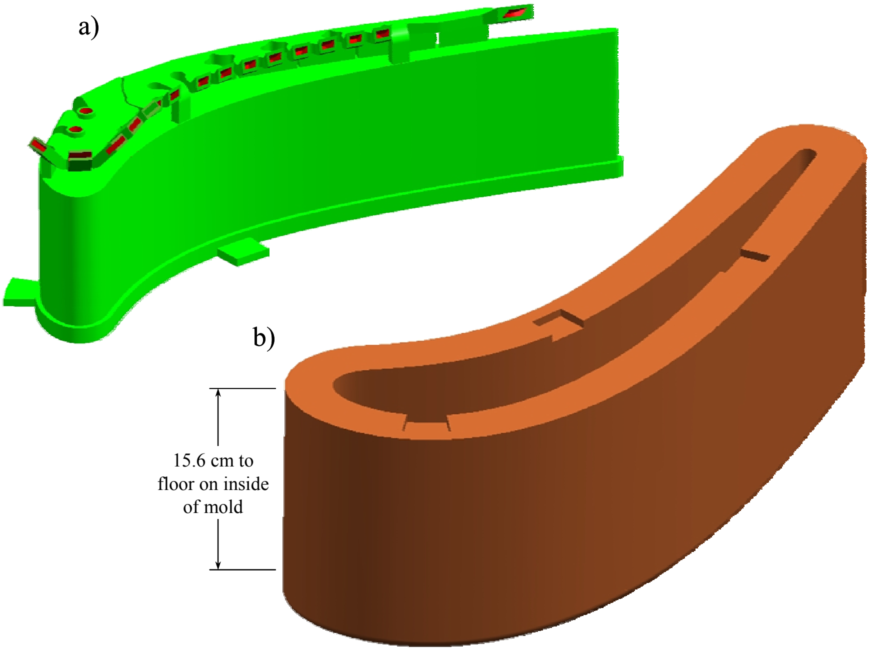

Figure 3-14 Models of the a) air passage piece and b) outer mold for the blade tip (Santeler, 2002).

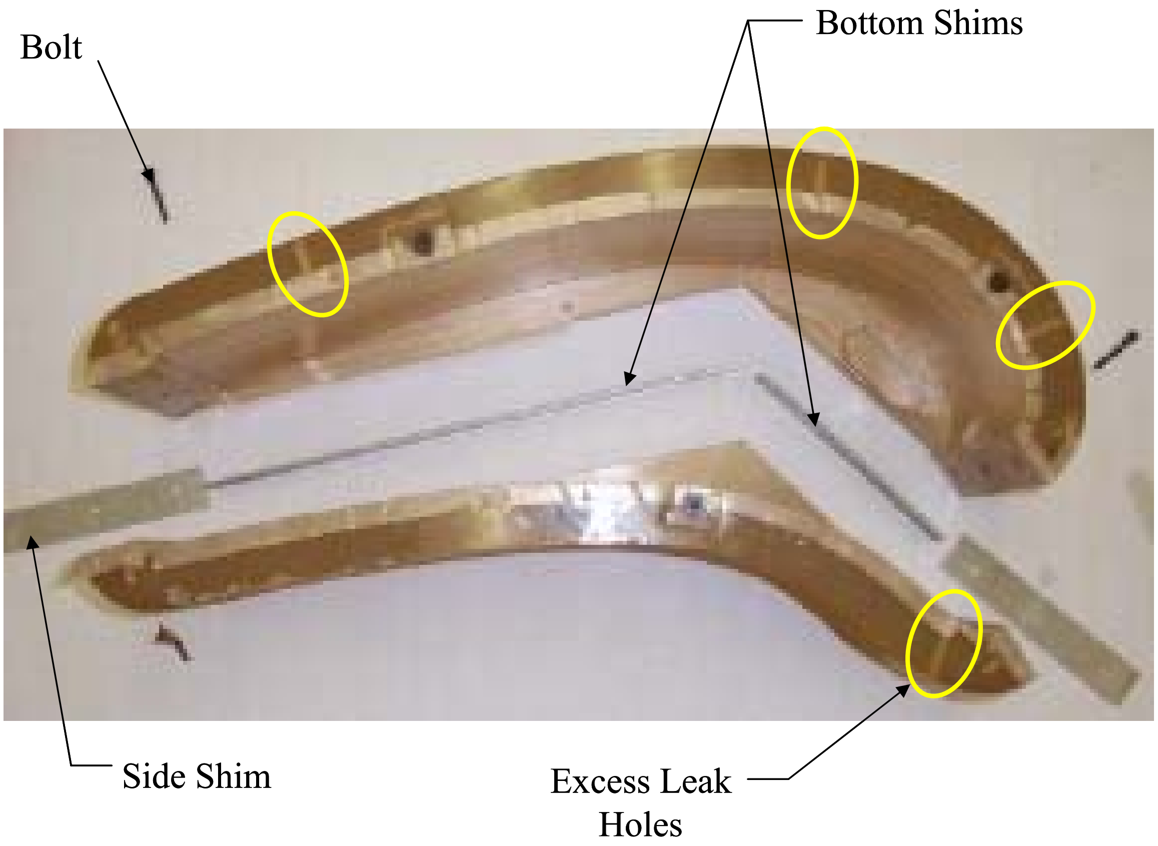

Figure 3-15 Two part outer mold assembly. Holes that were drilled to leak off excess foam are circled in yellow.

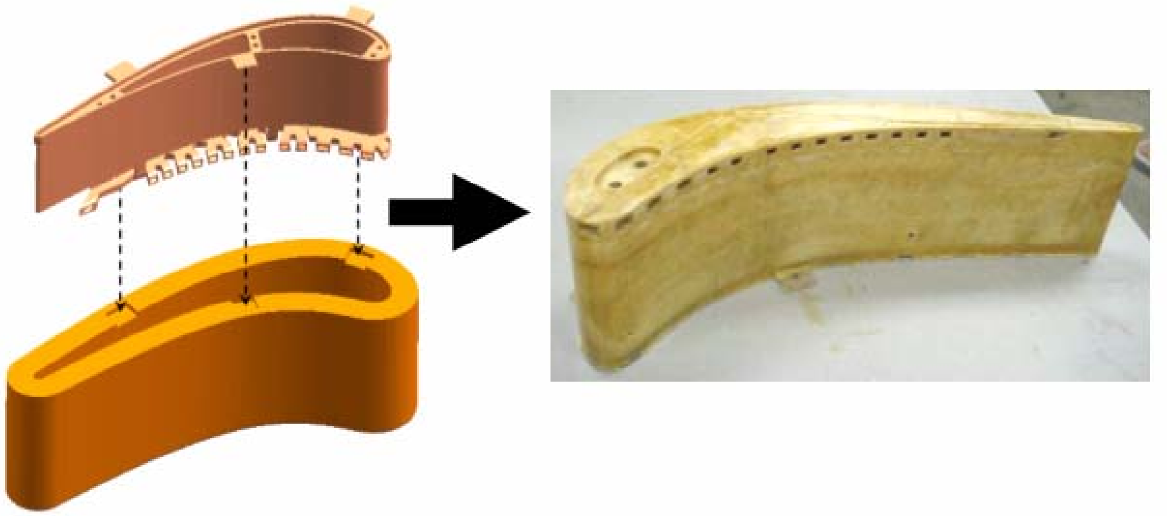

Figure 3-16 Final product of foam mold process.

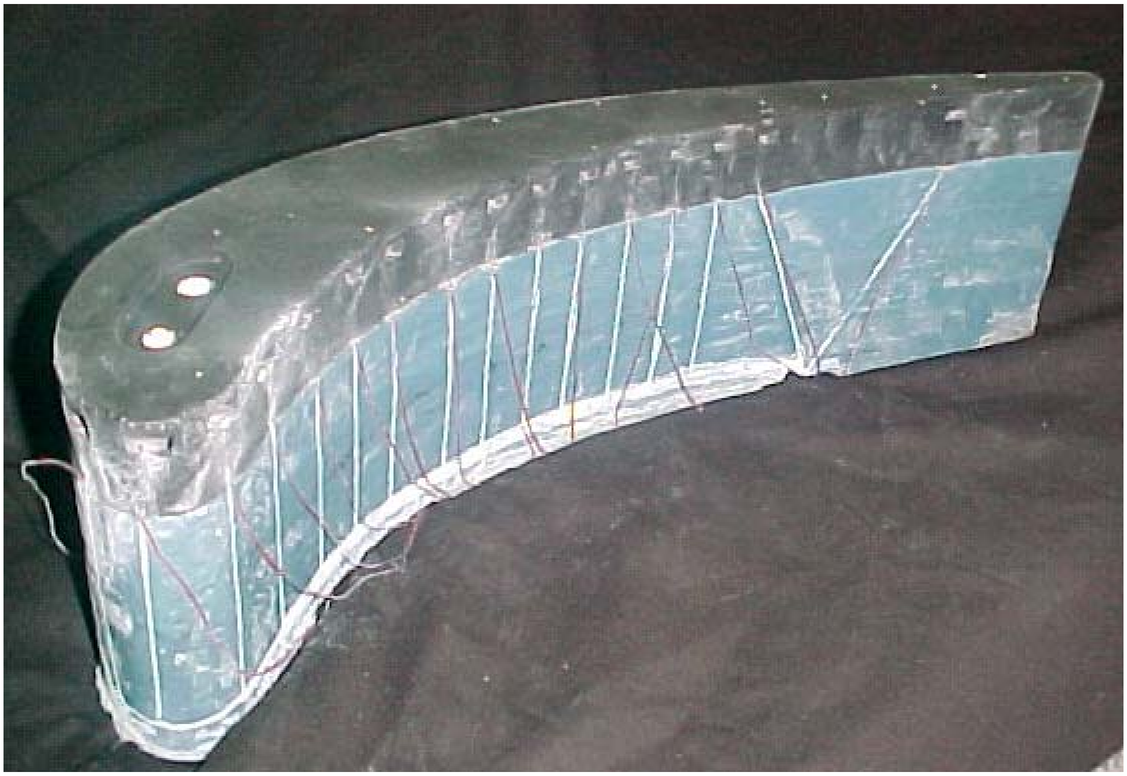

Figure 3-17 Final alumina tip model.

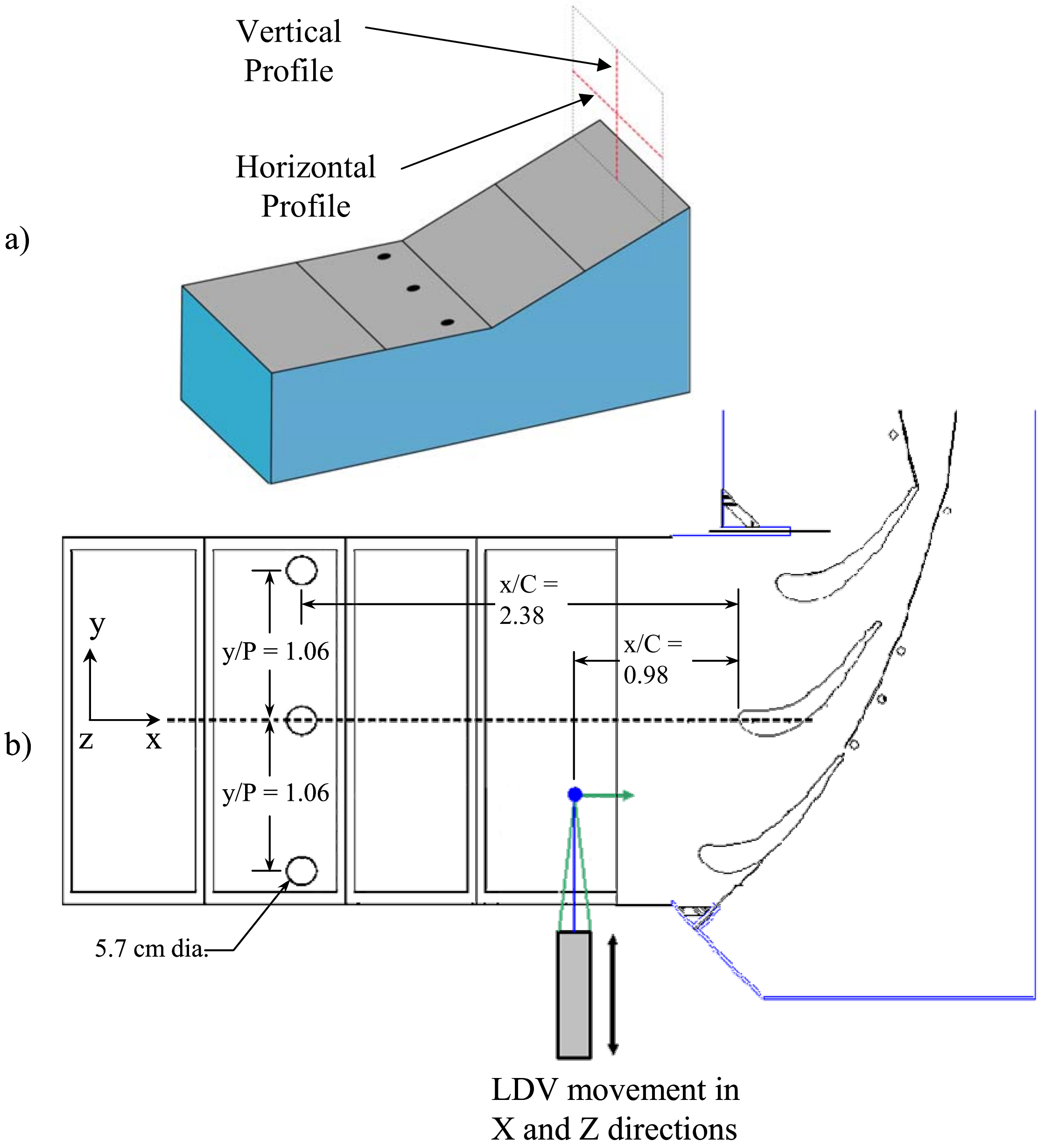

Figure 3-18 a) Horizontal and vertical velocity profiles measured upstream of the test section. b) Laser Doppler Velocimeter measures the z and x components of flow velocity upstream of the test section.

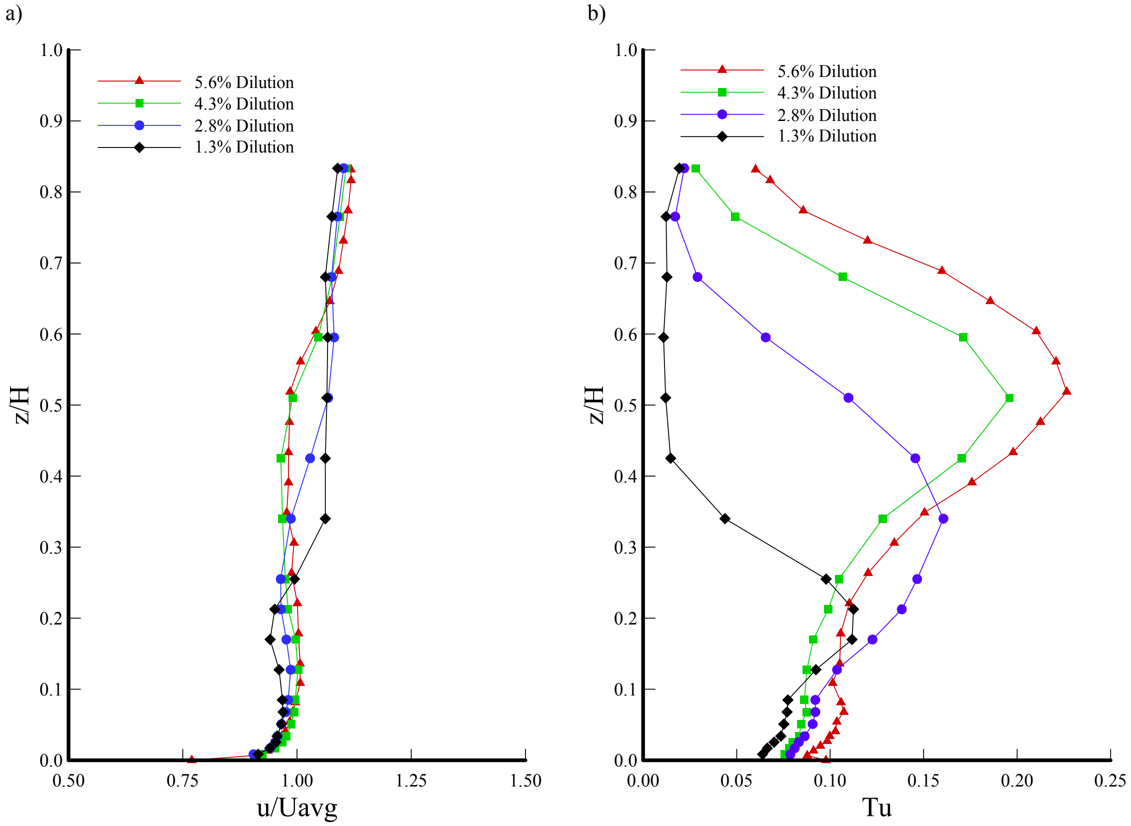

Figure 3-19 a) Vertical velocity profiles for four different dilution mass flow ratios and b) corresponding turbulence levels.

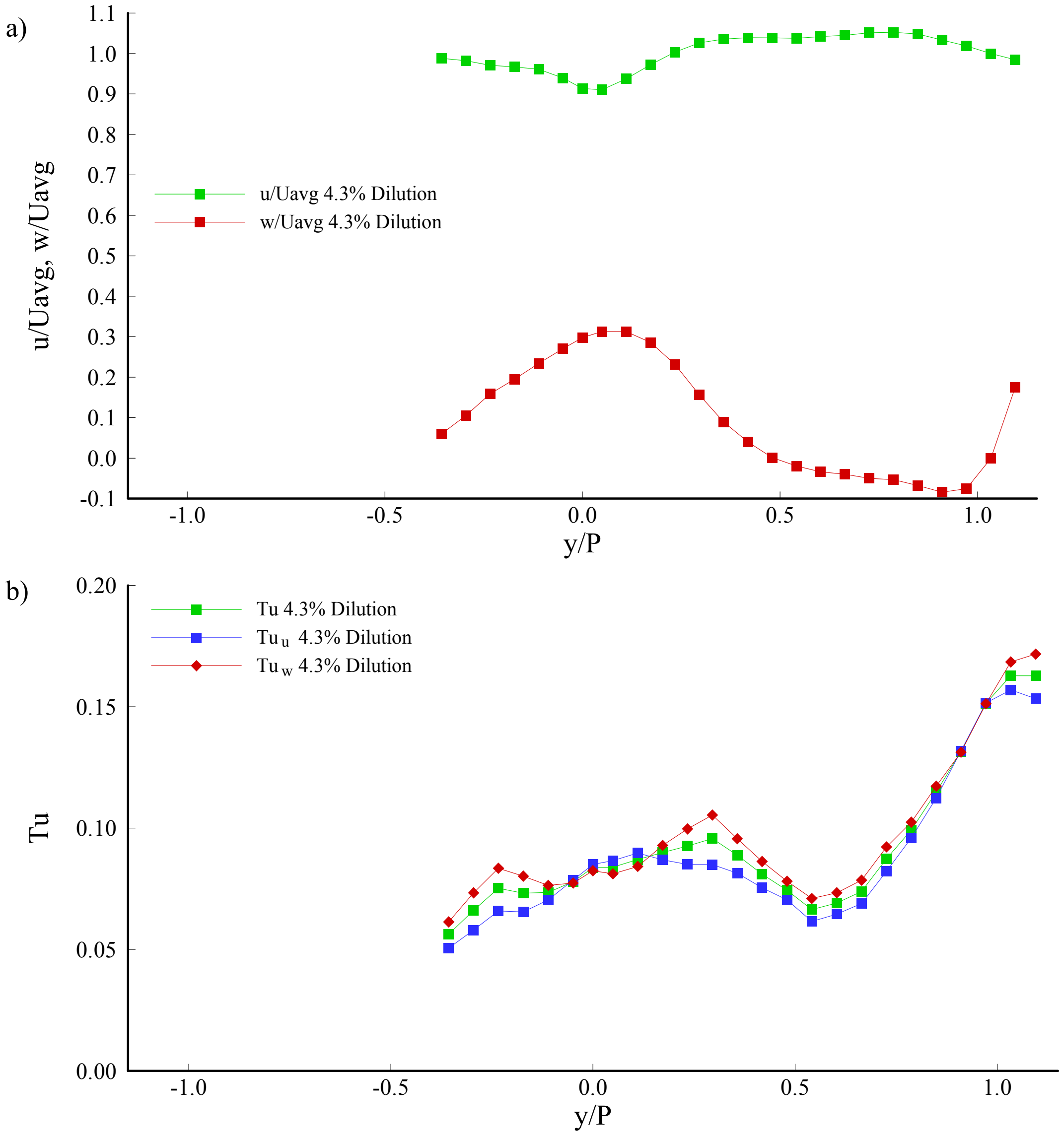

Figure 3-20 a) Horizontal profile of the cross-stream velocity component normalized by the free-stream mean velocity direction (w/Uavg) and the free-stream velocity component normalized by the free-stream mean velocity (u/Uavg) for 4.3% dilution flow. b) Horizontal profile of averaged turbulence levels (Tu), turbulence levels based on stream-wise fluctuations (Tu_u), and turbulence levels based on cross-stream fluctuations (Tu_w) for 4.3% dilution flow.

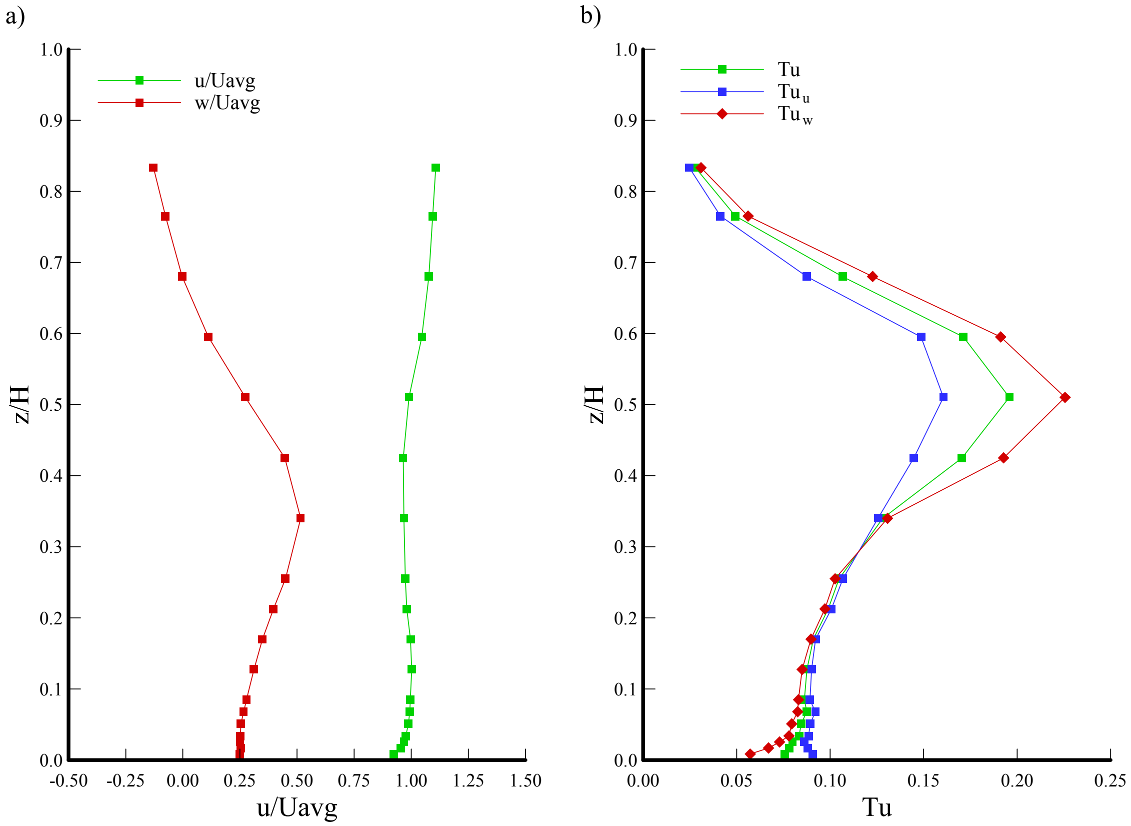

Figure 3-21 a) Vertical profile of the cross-stream velocity component normalized by the free-stream mean velocity direction (w/Uavg) and the free-stream velocity component normalized by the free-stream mean velocity (u/Uavg) for 4.3% dilution flow. b) Vertical profile of averaged turbulence levels (Tu), turbulence levels based on stream-wise fluctuations (Tu_u), and turbulence levels based on cross-stream fluctuations (Tu_w) for 4.3% dilution flow.

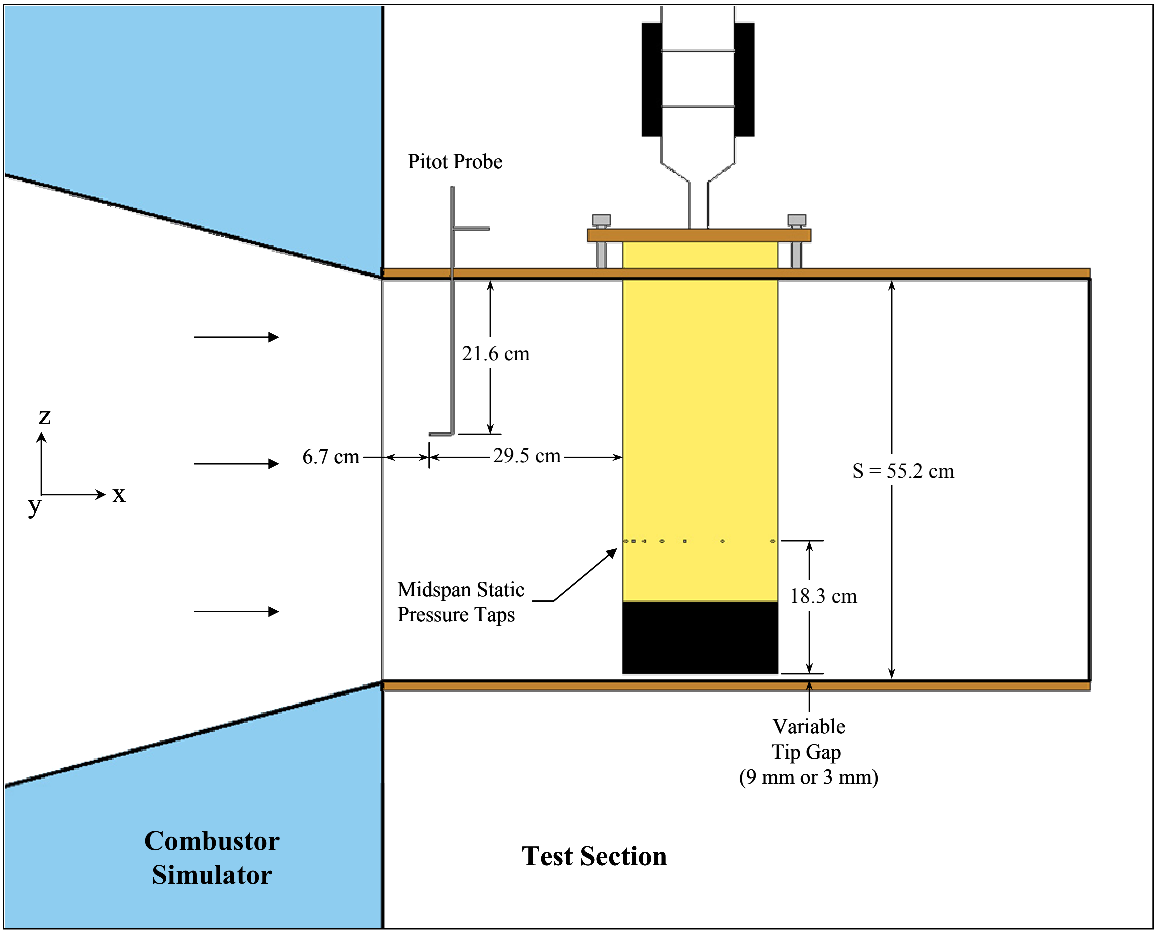

Figure 3-22 Side view of test section showing pitot probe location used to measure inlet velocity profiles. Dynamic pressure was measured at seven equally spaced locations in the y-direction.

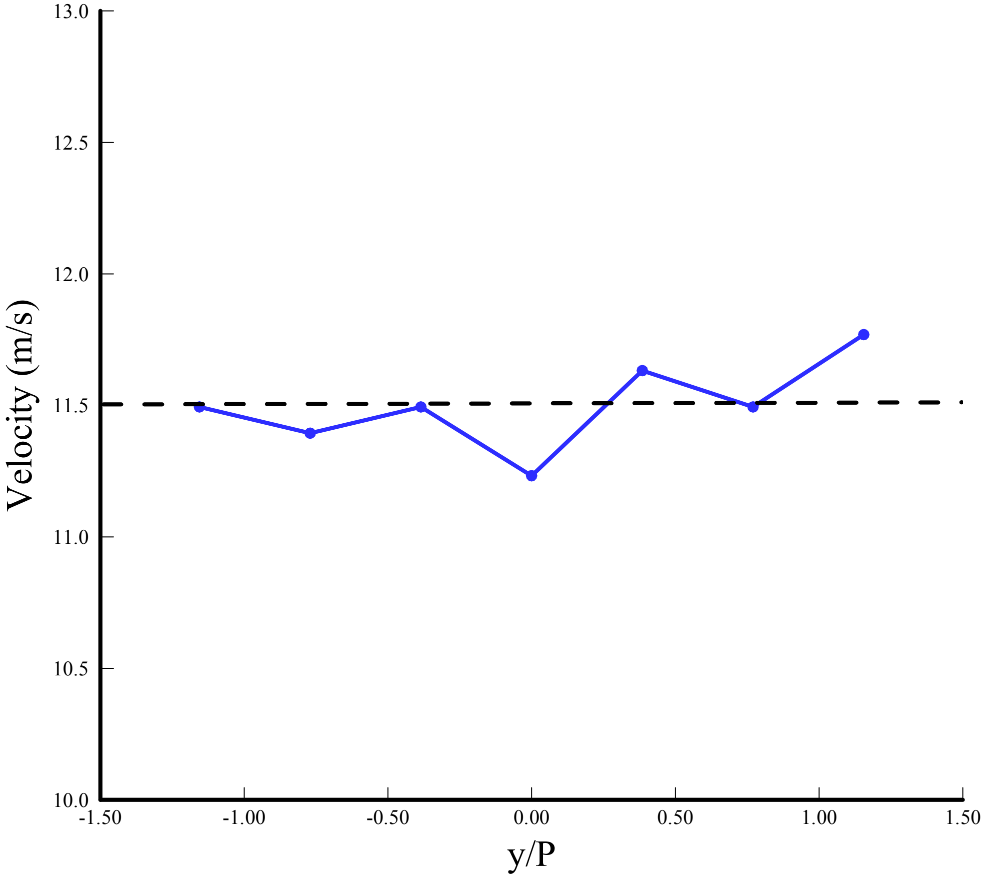

Figure 3-23 Sample of a horizontal velocity profile at the test section inlet. The dashed line is the mean velocity.

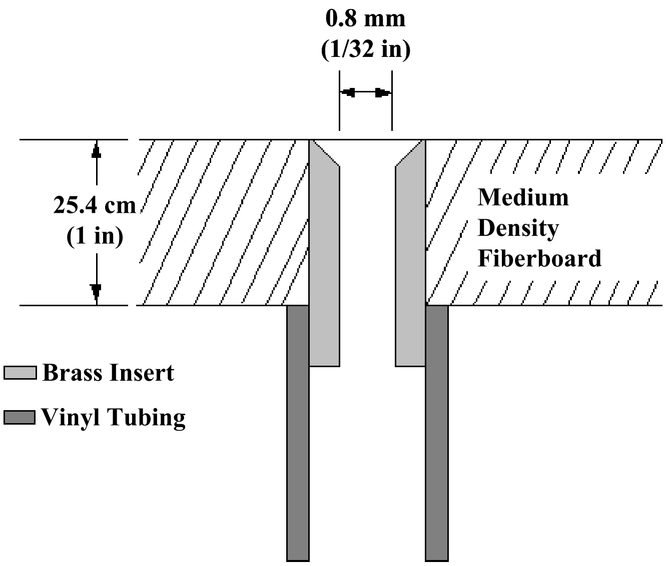

Figure 3-24 Static pressure tap configuration for pressure measurements on the shroud and midspan pressure measurements on the blade.

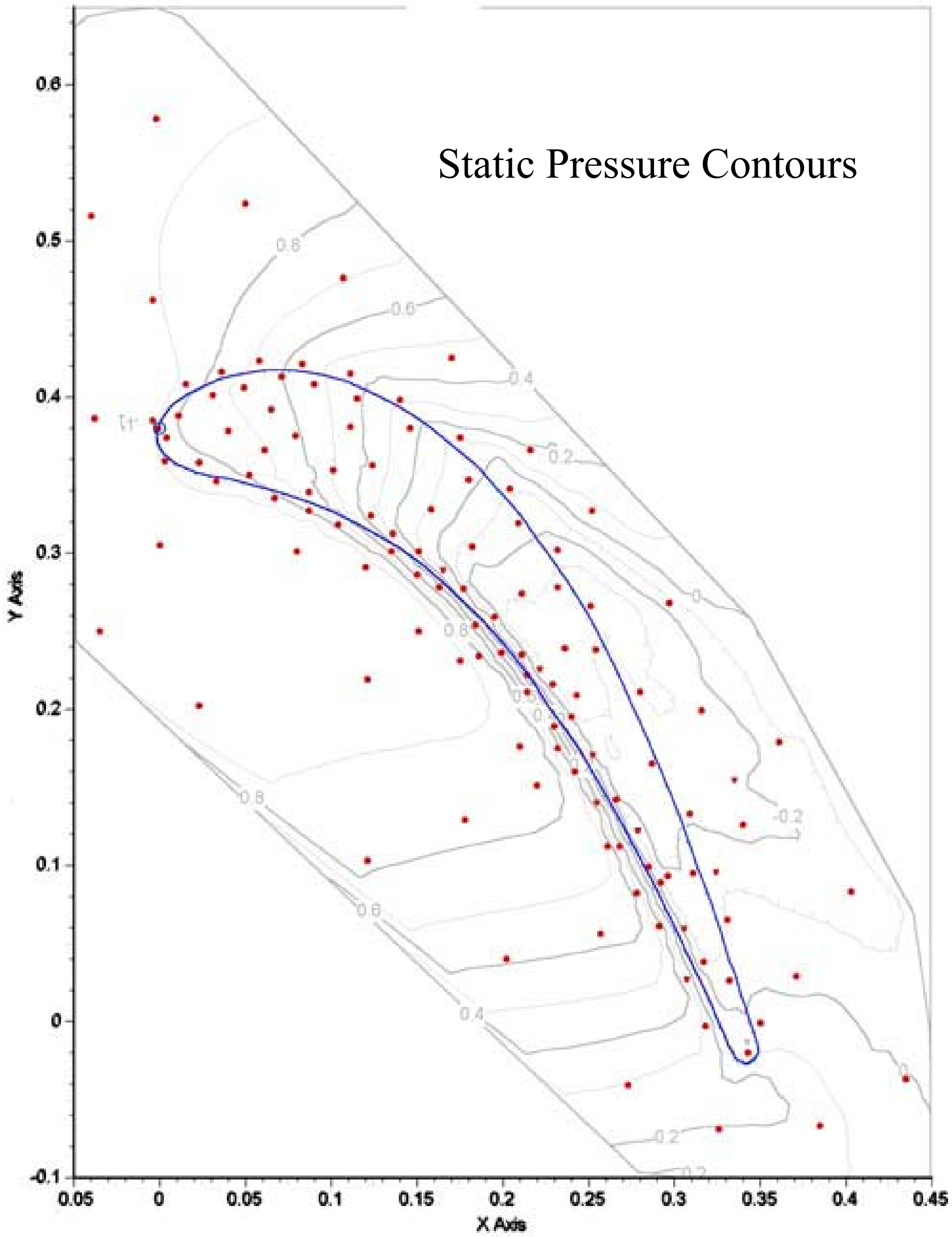

Figure 3-25 Static pressure tap array on the shroud overlaying shroud static pressure contours. The locations of the taps are indicated with red dots which were grouped around static pressure gradients (Christophel, 2003).

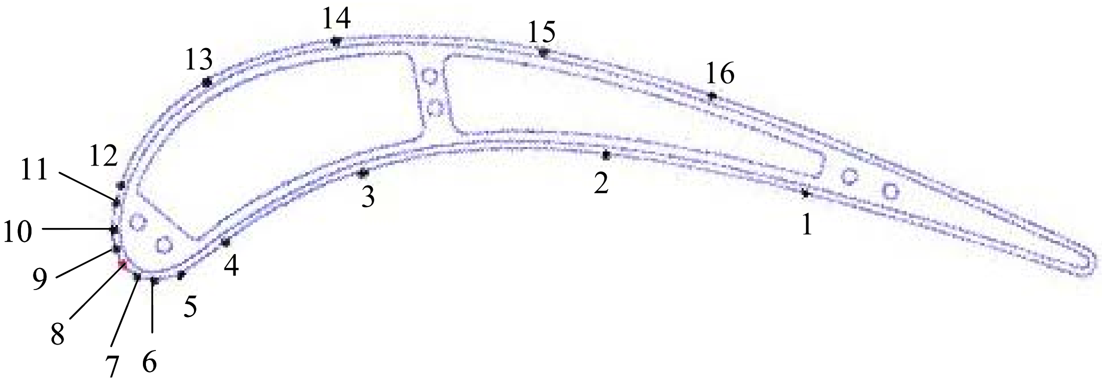

Figure 3-26 Static pressure tap locations on the blade midspan (Christophel, 2003).

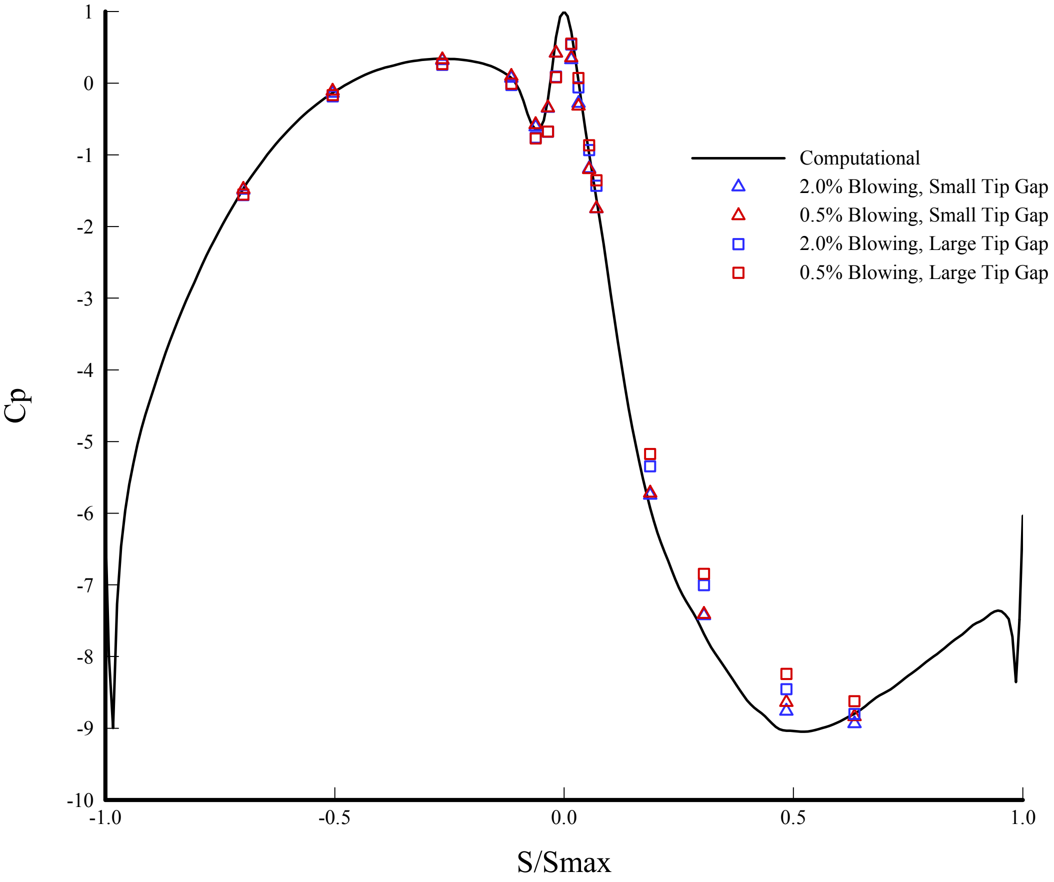

Figure 3-27 Comparison of experimental midspan pressure distribution to computational predictions.

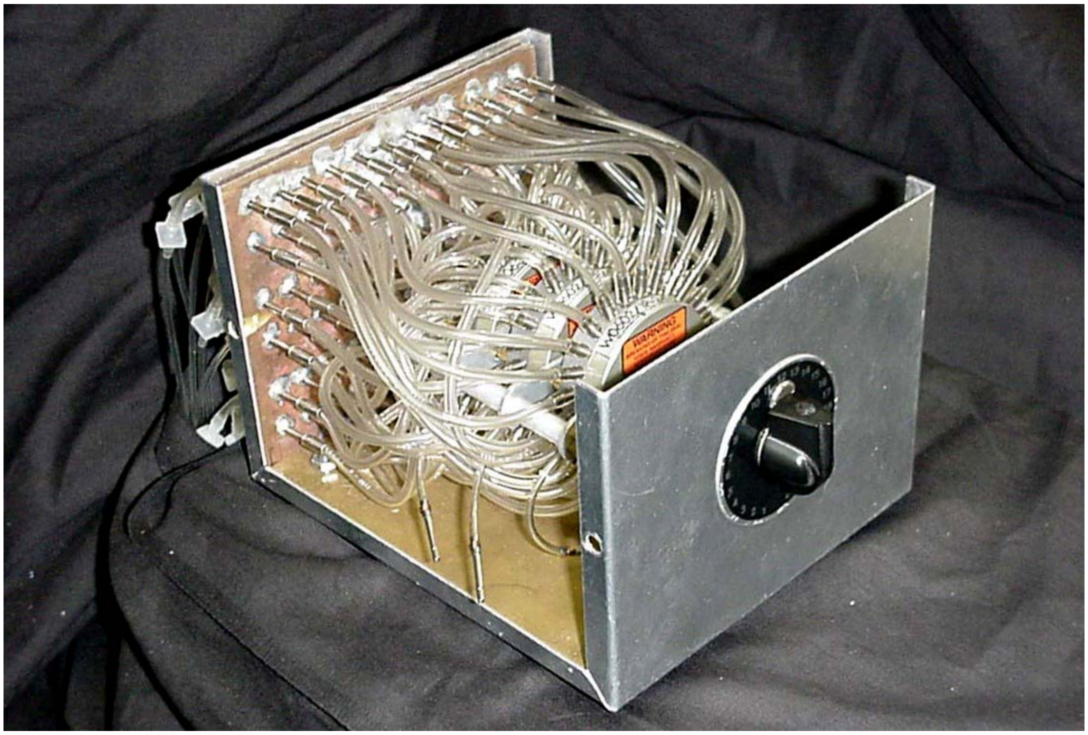

Figure 3-28 Scanivalve wafer and box (Vakil, 2002).

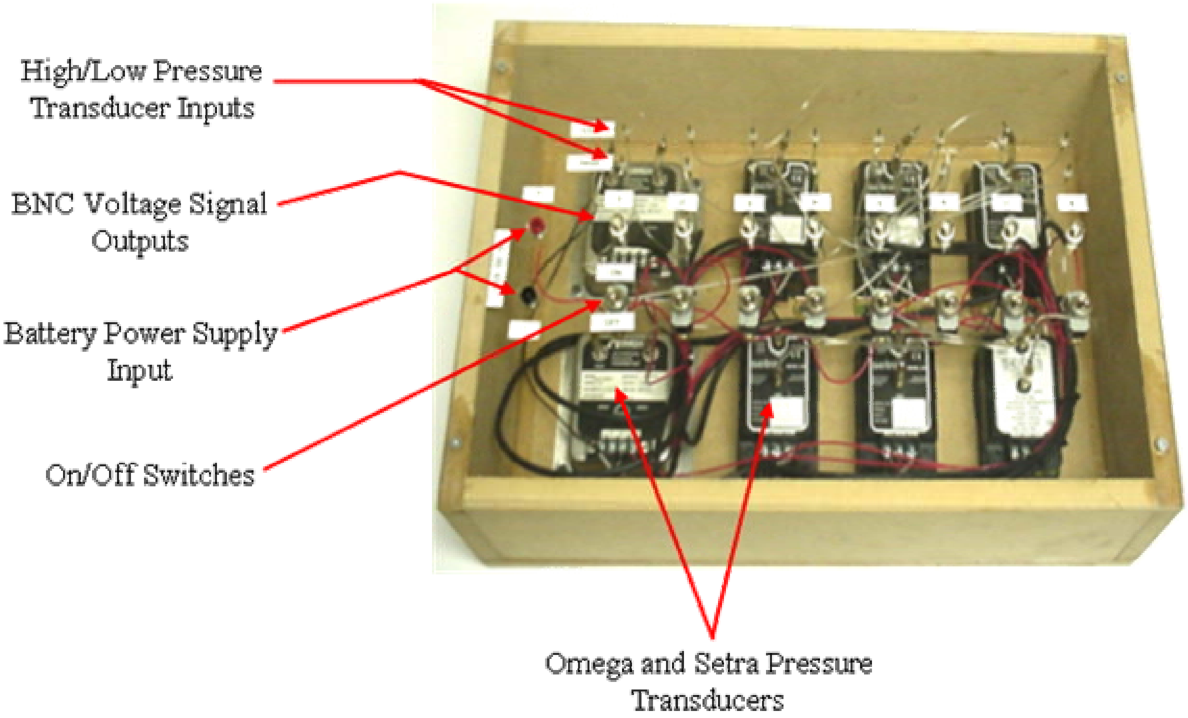

Figure 3-29 Transducer box. (Vakil, 2002).

Figure 3-30 Infrared camera.

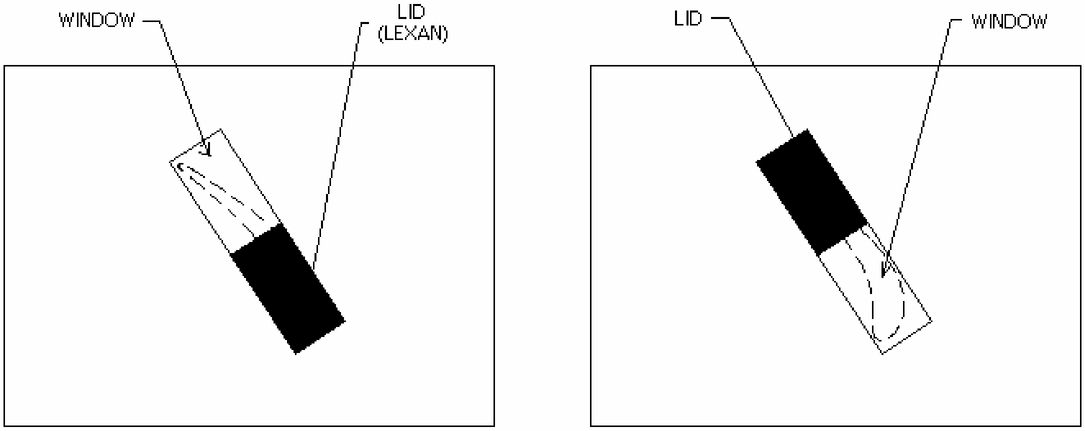

Figure 3-31 ZnSe window configurations to image blade tip.

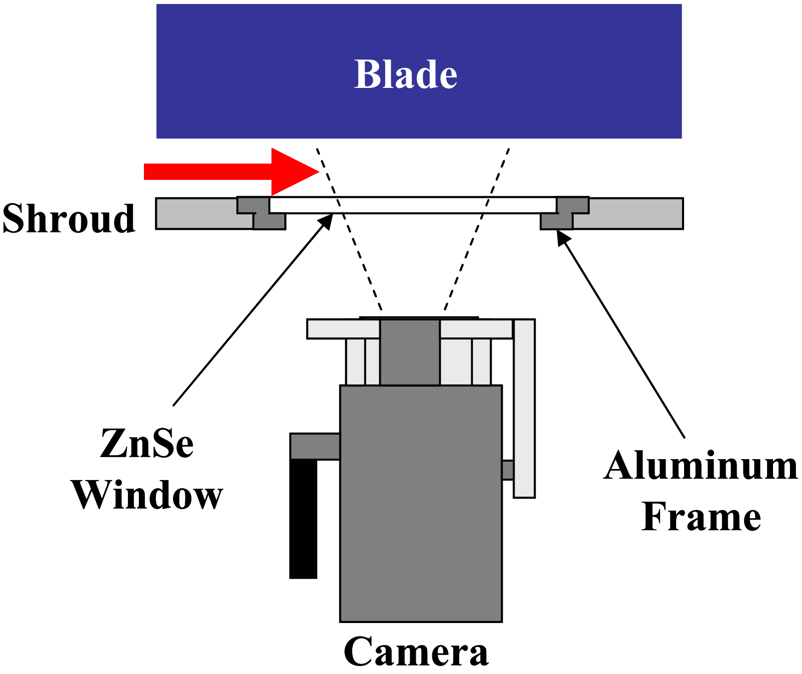

Figure 3-32 Infrared camera imaging the blade tip.

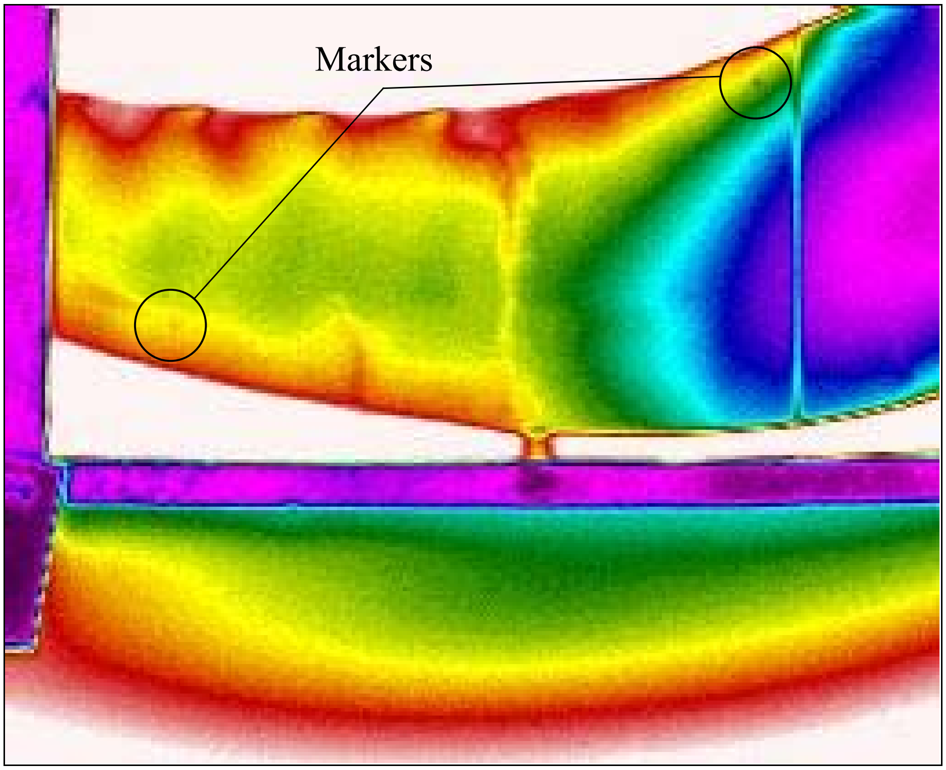

Figure 3-33 An infrared camera image of the alumina tip before any post processing.

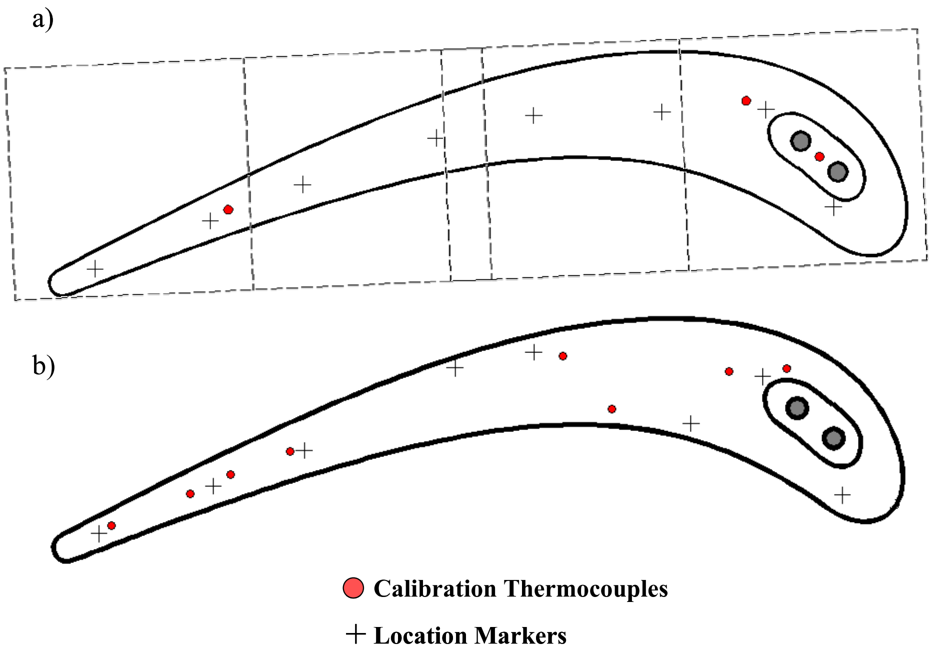

Figure 3-34 Marker and thermocouple locations for a) foam tip and b) alumina tip. The dashed lines show the areas that are imaged through the ZnSe windows.

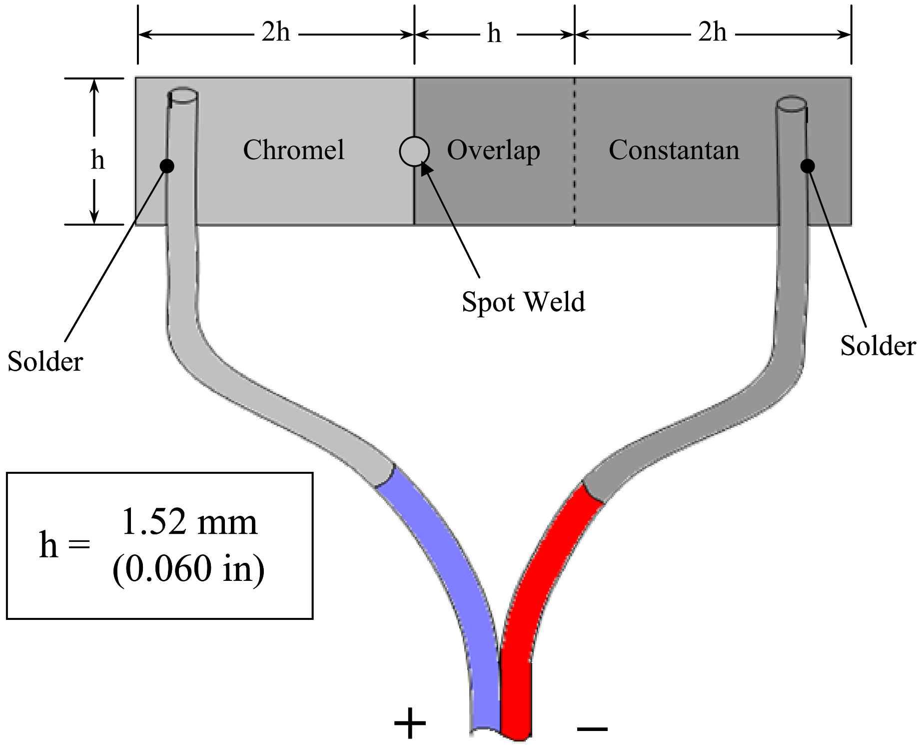

Figure 3-35 Layout of a thermocouple constructed from flat ribbons of chromel and constantan.

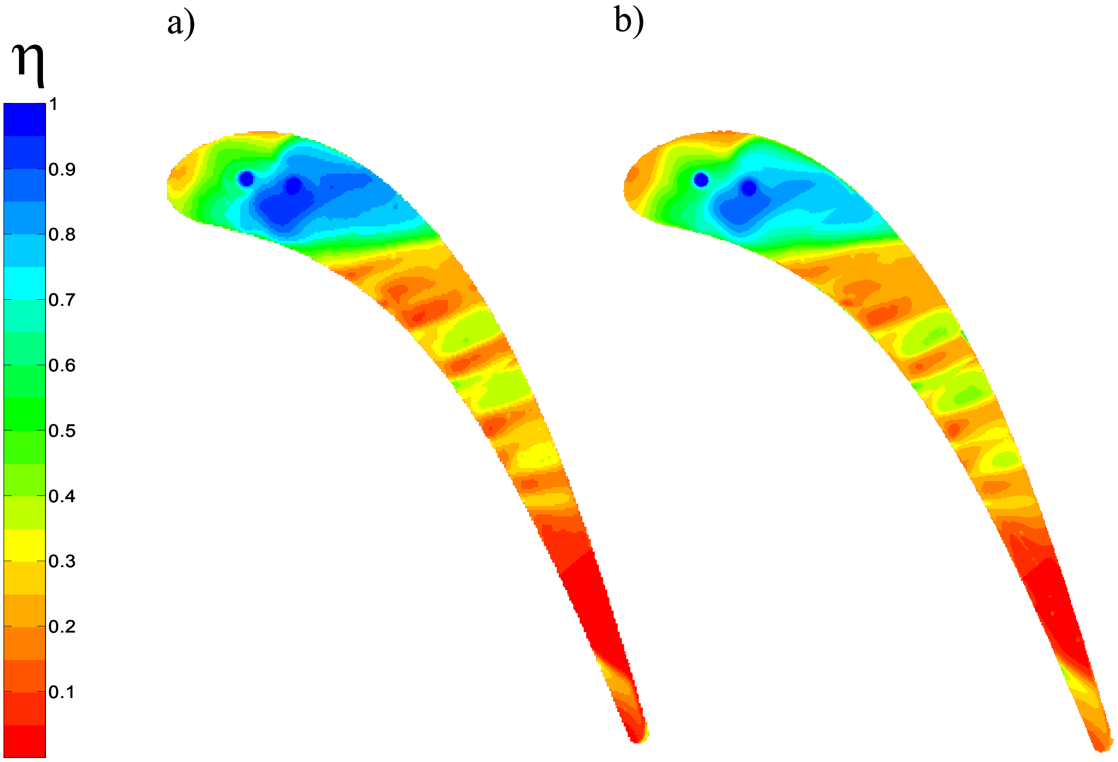

Figure 3-36 Repeatability results for adiabatic effectiveness. Tests were run with a large tip gap with 1.0% blowing from the microcircuit and dirt purge holes.

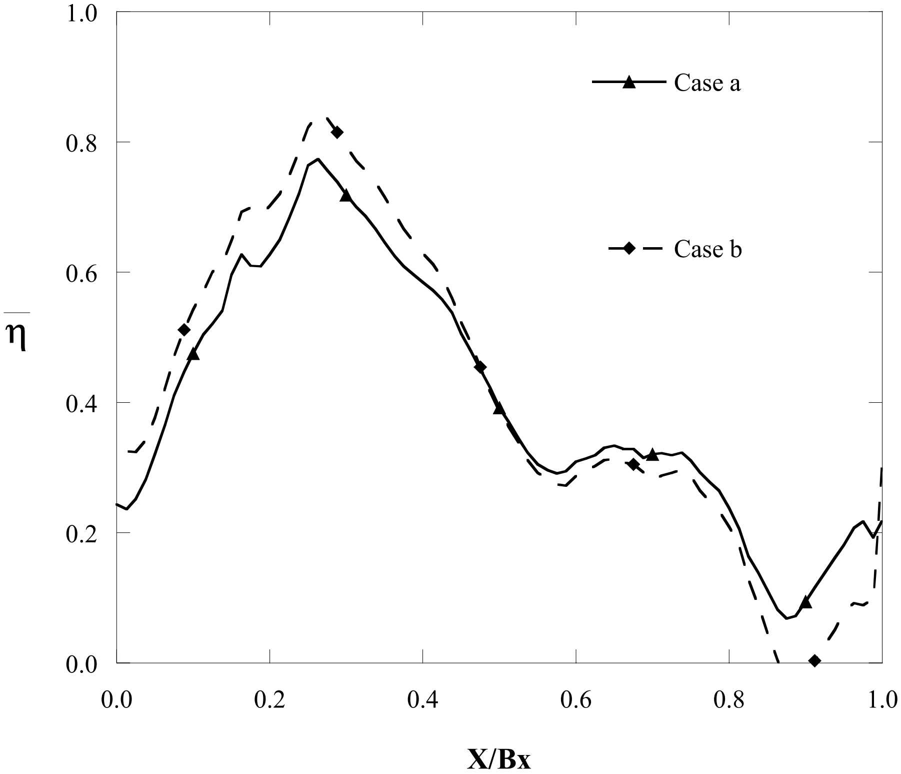

Figure 3-37 Lateral averages of the repeatability results for adiabatic effectiveness with a large tip gap at 1.0% blowing from the microcircuit and dirt purge holes.

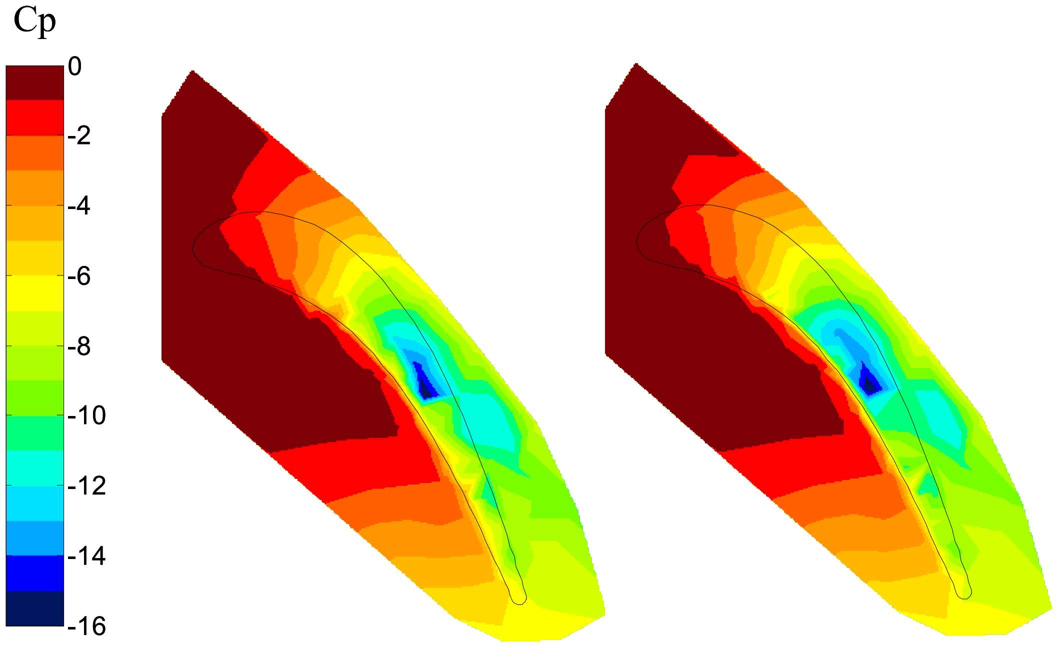

Figure 3-38 Repeatability results for pressure distribution on the shroud. Tests were run with a large tip gap with no blowing.